UCRL 2288

UNCLASSIFIED

UNIVERSITY OF CALIFORNIA

Radiation Laboratory

TWO-WEEK LOAN COPY

This is a Library Circulating Copy which may be borrowed for two weeks. For a personal retention copy, call Tech. Info. Division, Ext. 5545

BERKELEY, CALIFORNIA

DISCLAIMER

This document was prepared as an account of work sponsored by the United States Government. While this document is believed to contain correct information, neither the United States Government nor any agency thereof, nor the Regents of the University of California, nor any of their employees, makes any warranty, express or implied, or assumes any legal responsibility for the accuracy, completeness, or usefulness of any information, apparatus, product, or process disclosed, or represents that its use would not infringe privately owned rights. Reference herein to any specific commercial product, process, or service by its trade name, trademark, manufacturer, or otherwise, does not necessarily constitute or imply its endorsement, recommendation, or favoring by the United States Government or any agency thereof, or the Regents of the University of California. The views and opinions of authors expressed herein do not necessarily state or reflect those of the United States Government or any agency thereof or the Regents of the University of California.

UCRL-2288
Unclassified-Physics Distribution

UNIVERSITY OF CALIFORNIA

Radiation Laboratory

Contract No. W-7405-eng-48

TOTAL POSITIVE PION CROSS SECTIONS IN COMPLEX NUCLEI

Donald Harvey Stork

(Thesis)

July 27, 1953

Berkeley, California

TABLE OF CONTENTS

I	ABSTRACT	3
II	INTRODUCTION	4
III	MEASUREMENT OF THE CROSS SECTIONS	5
	A. Physical Arrangement and Procedure	5
	1. The Pion Beams	5
	2. The Counter System	8
	3. The Electronics	11
	4. Photographic Recording of the Data	12
	B. Reduction of the Data	13
	1. Pulse Height Selection	13
	2. Momentum Selection	14
	3. Targets	15
	4. Calculation of the Cross Sections	15
	C. Corrections	15
	1. Accidentals	15
	2. Pion-Muon Decay	16
	3. Multiple Coulomb Scattering	19
IV	THE MEASURED CROSS SECTIONS	21
V	THE COMPLEX SQUARE WELL MODEL	25
	A. General Description	25
	B. The Optical Model	26
	C. Coulomb Scattering	28
	D. Star Prong Correction	29
	E. Determination of the Inside Wave Number	30
	F. Energy Dependence of the Interaction Parameter and the Interaction Cross Sections	32
	G. Mean Free Path for Interaction in Nuclear Matter	34
	H. Relation to Interaction of Pions with Free Nucleons	35
VI	DISCUSSION	39
VII	ACKNOWLEDGEMENTS	43
VIII	REFERENCES	44

TOTAL POSITIVE PION CROSS SECTIONS IN COMPLEX NUCLEI

Donald Harvey Stork

Radiation Laboratory, Department of Physics
University of California, Berkeley, California

July 27, 1953

I ABSTRACT

The attenuation cross sections and cross sections for scattering into a ring counter were measured in a well defined geometry for positive pions of energies 33, 46, and 68 Mev. The targets were beryllium, carbon, aluminum, and copper. After correction for muon flux, accidentals, pion-muon decay, and multiple coulomb scattering, the results were analyzed in terms of a complex square well as treated by the optical model. The coulomb scattering and interference were calculated in the Born approximation. A strong energy dependence was found for the interaction mean free path in nuclear matter. The energy dependence for the mean free path, λ_a, was suggested to be given by

$$\lambda_a = \left[2b(kr_0)^4/\gamma^2\right]^{-1}$$

and b was found to be $0.21^{+0.04}_{-0.03}$. This was verified by a comparison of the optical model results with other published pion-nucleus interaction data. Good agreement was found with the least squares value for b given as 0.26 ± 0.02. The interaction mean free path thus derived was compared to that calculated by means of the multiple scattering theroy and the pion scattering amplitudes for the case of free nucleons. A rough agreement was found using the pion scattering phase shifts of Anderson, et al, and of Bodansky, et al.

TOTAL POSITIVE PION CROSS SECTIONS IN COMPLEX NUCLEI

Donald Harvey Stork

II INTRODUCTION

The total cross section for pions in complex nuclei may be considered to consist of two parts: an elastic or coherent scattering cross section, σ_s, and an interaction cross section, σ_a, that includes all processes, such as star formation, inelastic scattering, and charge exchange scattering, that remove pions from the coherent wave. Adopting a model in which the pion-nucleus interaction is represented by a complex square well, $V_r + iV_i$, of radius $R = (\hbar/m_\pi c)A^{1/3}$, an experimental measurement of σ_s and σ_a permits the determination of this complex well depth. It is expected that the behavior of the well depth with pion energy should reflect the characteristics of the pion-nucleon interaction.

The first experiments on pion cross sections in complex nuclei were performed by observing the interactions along both positive and negative pion tracks in nuclear emulsions[1, 2, 3] for pion energies between 30 and 100 Mev. The study was extended to pure targets with the cloud chamber experiments for 48 Mev[4] and 62 Mev[5] positive and negative pions using carbon as the target nucleus. Besides yielding the total cross sections, σ_s and σ_a, the above experiments gave additional information such as the star prong distributions and inelastic scattering from the nuclear emulsion experiments and the detailed angular distribution for the elastic scattering from the experiment of Byfield et al.[5] James Tracy[20] has recently made a cloud chamber study of the pion interaction in aluminum at several energies. Counter attenuation experiments as a function of A were done using negative pions by Chedester et al[6] at 85 Mev and by Martin[7] at 113 and 137 Mev. In the latter case the results were analyzed to give the interaction cross section, σ_a.

The counter attenuation and scattering experiment described in this paper is intended to extend the pion-nucleus cross section data to lower energies in order that a better understanding of the behavior of the pion-nucleus interaction may be obtained.

III MEASUREMENT OF THE CROSS SECTIONS

Three pion energies were chosen for this study: 33, 46, and 68 Mev. The target nuclei were beryllium, carbon, aluminum, and copper. To distinguish the pions from the background, a momentum selection and pulse height analysis were made. The attenuation cross sections for the various targets and at the three pion energies were measured in a well defined geometry. The cross sections for pion scattering into a ring counter were obtained simultaneously.

A. Physical Arrangement and Procedure

1. The Pion Beams. Two criteria were used in making the pion beams. First, it was required that the pion flux should be sufficient and the background small enough to make the measurements obtainable in a reasonable length of time. Secondly, the energy spread of the pion beam was required to be small enough so that an energy dependence to the cross sections could be clearly established. In the arrangement that was used, background problems were easily handled and the pion energies were sufficiently monochromatic, but the flux was small, so that only a crude measurement of the scattering cross section at one angular interval could be obtained.

The general physical arrangement for the experiment is shown in Fig. 1. The pion beams were produced by bombarding either a polyethylene or a carbon production target by the 340 Mev external scattered proton beam at the 184-inch synchrocyclotron. The target was placed in the 5 inch gap of a large pair spectrometer magnet. Pions produced in the forward direction were bent through an arc of 90° in an 18.5 inch radius, leaving the magnet gap through a brass slit in a direction 35° to the normal of the magnetic field boundary. The pions continued through a hole in the five foot thick concrete shielding and passed through a collimating counter inside the shielding and into the main counting system just outside the shielding. The geometry of the beam was such that because of the properties of the fringing field at the exit of the magnet gap, a first order focus of the pion beam in the vertical plane was obtained. Thus, in the vertical plane, a pion image at the counter system was formed of the proton beam at the production target. This effect was verified experimentally by observing the counting rate as the magnet was raised and lowered.

The external scattered proton beam left the vacuum system of the synchrocyclotron as a sharp, nearly horizontal line. After leaving the vacuum system the proton beam traveled ten feet before striking the pion production target. Multiple coulomb scattering in the exit window and in the air distorted the line characteristic of the proton beam in this distance. Consequently, a temporary extension of the cyclotron vacuum system back to the magnet was used to preserve the sharpness of the horizontal line of the proton beam. The decreasing of the vertical dimension of the proton beam at the production target served to decrease the vertical dimension of the pion image at the counting system. Thus, by means of this arrangement, an increase in pion flux of a factor of about two was obtained.

The definition in pion beam energy was provided by the momentum selection determined by the production target width and position, the field exit slit width and position, and the position of the counters. With a production target 1-7/8 inches wide, slightly narrower than the proton beam, and an exit slit width of 1-7/8 inches, the momentum interval for pions capable of leaving the target and passing through the exit slit in the direction of the counters was small enough to give a satisfactory energy resolution to the beam. This was chosen as an optimum balance between energy resolution and pion flux.

For the two low energy pion beams a polyethylene production target was used to take advantage of the large cross section for the reaction $p + p \rightarrow \pi^+ + d$.[8] This gave monoenergetic pions in the forward direction, and the energy of the pion beam was adjusted by varying the thickness of the polyethylene target. Pions leaving the thick target also remained monoenergetic, because of a compensating action described elsewhere,[9] but were degraded in energy. In practice, to obtain the desired pion beam energy, the thickness of polyethylene target required was computed from the stopping power of polyethylene, the kinematics of the reaction $p + p \rightarrow \pi^+ + d$, and an approximate knowledge of the proton beam energy. The counting rate was plotted as a function of magnetic field. A sharp peak appeared when the magnetic field was at the correct value to direct the pions from the reaction $p + p \rightarrow \pi^+ + d$ through the slit system in the direction of the counters. The magnetic field was set for the peak flux and the energy distribution of the resulting pion

beam was determined by using copper absorbers to measure the pion range distribution. Generally, the energy differed from the desired value by a few Mev and the polyethylene production target thickness was adjusted accordingly and the above process repeated. To determine the absolute energy of the pion beams, integral range curves were measured. To obtain the energy distribution of the pions in the beam, differential range curves were run.

The highest energy could not be reached with the reaction $p + p \rightarrow \pi^+ + d$, so a 2 inch carbon production target was used in this case. Here, the pions are produced over a broad spectrum[10] and the magnetic field was set to bend pions of the appropriate energy through the field exit slit as determined by wire trajectory measurements. A range curve was plotted and, if necessary, the field was changed to give the desired energy and the range measurements were repeated.

The energy was measured both before and after each run and in no case was a change in energy found, although there was evidence of a small change in proton beam energy from one run to the next. In Fig. 2, the pion energy spectra of the three beams are shown. These were determined by range in copper with a pulse height selection of the pions that will be described later. As the pions entered the attenuation target, after passing through the collimating, pulse height, and passing counters, the three pion beam energies and half widths at half maximum were 37.5 ± 4, 51 ± 3, and 73 ± 8 Mev. For the two lower energies, most of the pions were from the reaction $p + p \rightarrow \pi^+ + d$ and the energy distribution was somewhat sharper than that defined solely by the momentum selection provided by the geometry of the production target, exit slit, and counters. The geometric momentum selection was quite necessary, however, to limit the energies of pions produced in the carbon in the polyethylene target. For the high energy beam, in which a carbon target was used, the energy distribution was determined almost entirely by the geometric momentum selection.

The pion beam flux at the counter system varied between one and two pions per square inch per second. This low flux required an efficient method of taking data. Such a method was found in the photographic recording method to be described later.

2. The Counter System. The geometry and some of the details of construction of the counter system are shown in Fig. 3. The beam passed first through a collimating counter consisting of a 1/8 inch thick, 1-1/2 inch square anthracene crystal viewed through a short lucite light pipe by a 1P21 photomultiplier. The beam next passed through the pulse height counter which consisted of a 1/2 inch thick, 1-1/4 inch square stilbene crystal viewed on two sides through short lucite light pipes by 5819 photomultipliers. A cylindrical 2 inch diameter aluminum foil reflector provided maximum light collection. Short signal leads from the two 5819's were simply connected together at a coaxial tee and the tubes were matched in gain by suitably adjusting their voltages. Stilbene was chosen principally for its availability in a clear form at the time of construction. It was found that the two photomultipliers provided slightly better pulse height resolution than a single photomultiplier with a reflector at the opposite end of the crystal. This is thought to be due to an improvement in uniformity of light collection across the crystal rather than an increase in light collection. The third counter that the pion beam passed through was simply a passing counter, similar in construction to the pulse height counter. The crystal was stilbene, 1/4 inch thick and one and 3/16 inches square. Immediately following the passing counter was the attenuation and scattering target.

Lastly was the back counter which consisted of a 14 inch diameter liquid scintillating solution 1/2 inch thick. The solution was terphenyl in phenylcyclohexane with the red shifter, diphenyl hexatriene, added. It was contained in a 12 mil aluminum foil sealed to an aluminum ring by means of thermal setting araldite. The back face was a 1/4 inch lucite plate sealed to the aluminum ring by cold setting araldite and clamped for mechanical strength. The 14 inch diameter scintillator was divided into two sections by means of aluminum foil light baffles and reflectors placed behind the lucite back face. In this way an inner 8 inch diameter circle was viewed by four 5819 photomultipliers and an outer 3 inch ring was viewed by six 5819 photomultipliers. Signal leads from the inner four 5819's were connected together to a single coaxial connecter and leads from the outer six 5819's were connected together to a second coaxial connecter. In this way separate signals from the two sections of the back counter could be obtained.

Because of the overlap in light collection, the full 14 inch diameter could be used with no blind spots for attenuation cross section measurements. The ring section was originally designed to determine emperically the effect of multiple coulomb scattering, but was later found suitable for crude measurements of the scattering cross sections. Particles passing through the scintillator near the division between the inner and outer sections gave rise to a pulse from both sections. However, by the establishment of a pulse height criterion for deciding which side of the division the particle passed through, the separation became satisfactorily distinct.

Because of the smallness of the effects being measured, it was required that the back counter be essentially 100 percent efficient. In a trial model in which a solution of terphenyl in xylene viewed by 1P21 photomultipliers was used, an efficiency of less than 90 percent was obtained. By examining the pulse height distribution it was found that this was due to poor light collection. The number of photoelectrons leaving the photosensitive surface in the photomultipliers was so small that statistical fluctuations gave rise to a significant number of statistically zero pulses. This situation was corrected by the improved light collection in the final model. By examining the pulse height distribution, the number of statistically zero pulses was found to be completely negligible.

To insure maximum collection of primary photoelectrons in the photomultipliers, the voltage between photocathode and first dynode was twice that between each succeeding pair of dynodes. The response of each tube in the back counter was measured as a function of voltage by means of a Ra-Be source and an ultra-sensitive microammeter that was used to measure the anode current due to scintillation of the liquid scintillator in the presence of the source. Thus the response of the tubes could be matched by suitably adjusting their individual voltages. By the same technique the uniformity of the back counter across its face could be determined. Both the inside section and the outside ring section had a response uniform to about 10 percent. The response was periodically checked with no significant change being found.

The pion beam direction was defined by the exit slit and front counters to within limits of $1\text{-}1/2^{\circ}$. The collimating counter was two

feet in front of the pulse height counter to reduce random direction background. The counters themselves thus defined the direction of the beam to within limits of 3°. Multiple coulomb scattering in the crystals, although small, tended to reduce the angular definition provided by the exit slit and counter geometry.

The special purpose of the pulse height counter was to provide a pulse height selection as an aid in distinguishing pions from the background. This will be described in detail in a later section. The passing counter was used only to form a coincidence with the collimating and pulse height counters. Since the crystal subtended a fairly large solid angle in the backward direction from the attenuation target, some of the back scattering and star prongs from the target traveled back through the passing crystal and the passing counter was not used for pulse height selection in order that these events should not be lost. This effect was negligible in the case of the pulse height counter because of the increased separation between it and the target.

An attenuation event was defined as an event in which a particle that had passed through the front three counters failed to reach either section of the back counter. A ring counter event was defined as one in which a particle traversed the front three counters and appeared to pass through the ring section of the back counter, the pulse height criterion being used if pulses from both the inside and outside sections of the back counter were present. Since the pion beam was of finite extent, it was required that the back counter be large enough so that the geometry was well defined. The angular efficiency of the back counter as a whole and of the ring counter section is shown in Fig. 4 for the two geometries that were used in the present experiment. For most cases the 10 inch separation from target to back counter was used giving half angles of 21.7° and 35° for the two back counter boundaries. These angles will be referred to hereafter as α_1 and α_2 respectively. In the case of the aluminum and copper targets at the low energy, multiple coulomb scattering required both a reduction in target thickness and an increase in the angle subtended by the back counter. Therefore, in this case, a separation of 7-3/4 inches was used resulting in half angles of 26.6° for α_1 and 42° for α_2.

3. The Electronics. A block diagram of the electronics is shown in Fig. 5. Pulses from the pulse height and passing counters were lengthened by a condenser-resistor network and clipped at 0.25 microsecond by means of a shorted RG63/U cable in order to insure stable operation of the feedback principle in the linear amplifiers. Pulses from all counters were amplified by linear amplifiers. The amplified pulses from the front three counters triggered variable gates which put out square, 25 volt pulses of 0.5 microsecond duration. These were mixed in a coincidence unit whose output was a 20 volt, one microsecond square pulse. This output was fed into the trigger input of an oscilloscope.

From the second cathode follower output of the linear amplifiers for all but the collimating counter, the pulses were fed through different lengths of RG65/U cable to a funnel circuit. The funnel circuit consisted of four impedance-matched input voltage dividers and four 6AG7 feedback amplifier stages with a gain of two and with the plates connected in parallel. The output from the common plate terminal was connected to the signal input of the oscilloscope. The purpose of the funnel circuit was to bring the four signals together at the oscilloscope while providing separate attenuation controls and proper impedance matching for the delay line RG65/U cables. A Tektronix type 511A oscilloscope was used, modified for a 5XP11A cathode ray tube with a 12 KV supply. All of the principal electronics units except the funnel circuit and the oscilloscope were standard equipment maintained in the counting area at the synchrocyclotron.

The operation of the electronics was as follows. If a particle passed through the front three counters, a coincidence was formed with the coincidence output triggering the oscilloscope sweep. Pulses from the pulse height counter, the passing counter, and from either section of the back counter, if present, appeared across the oscilloscope trace separated by means of the different lengths of RG65/U delay lines. By means of test pulses it was found that the height of the pulses appearing on the oscilloscope trace were quite linearly proportional to the signals at the input of the linear amplifiers. Furthermore, it was found in tests with the proton beam and in the actual running with the pion beams that the pulse heights on the oscilloscope trace were linearly proportional to the energy loss of the particle in the counters.

4. Photographic Recording of the Data. The oscilloscope traces were photographed on continuously moving Kodak Linagraph Pan 35 mm film by means of a General Radio camera. After a run was completed, the film was processed and the images of the oscilloscope traces were examined through the use of a Recordak microfilm viewer. Measurements of the positions of the pulses along the trace and of the height of the pulses could be made by projecting the image on ordinary graph paper. A sample strip of the film is reproduced in Fig. 6. The traces represented a time duration of about five microseconds and were 10 cm in length on the oscilloscope face. Reading from left to right in Fig. 6, pulse number one is that from the pulse height counter. The second pulse appears at a time 0.84 microsecond after the first and is from the inside section of the back counter. Pulse number three, when present, appears 1.64 microseconds after the first and is from the outer ring section of the back counter. The last pulse is from the passing counter and appears 2.60 microseconds after the first. The separation of the pulses was obtained by the different length of delay line used for each signal. The scale by means of which the separation of the pulses was measured could be converted to a time measurement and it was found that the separation of the starting points of the pulses could be readily determined to within 0.04 microsecond. Consequently, this time could be considered to be the effective resolving time for determining coincidences. The scale with which the pulse heights were measured was divided into one hundred divisions with a reading resolution of one division. The pulse height distribution peak for the pulse height counter was generally near 30 divisions in height.

The principal purpose for using this photographic method of recording data was the simplicity with which a large amount of detailed information could be permanently recorded. The price that was payed for the resulting efficiency in running time was the tedious labor that was involved in analyzing the film. The number of events was determined by examining each image of the oscilloscope traces. An attenuation event was one in which the pulses from both sections of the back counter were missing. A ring counter event was one in which the pulse from the inside section of the back counter was absent while that from the ring section was present, or, in cases where the particle passed near

the division between the two sections of the back counter, one in which the pulse from the ring section was larger than a certain minimum pulse height, while that from the inside section was smaller than a certain pulse height. Examples of events are found in Fig. 6. The third trace from the bottom in the figure is an attenuation event and the bottom trace is a ring counter event.

B. Reduction of the Data

1. Pulse Height Selection. By examining the pulses on the projected image of the traces on the film, relative pulse height measurements could be made. As was mentioned, pulse height measurements of the back counter pulses were sometimes used for the criterion for ring counter events. Also the good efficiency of the back counter was verified by examining the pulse height distribution for the back counter. The principal use of pulse height measurements, however, was to aid in the separation of the pions from the background. For this purpose the heights of the pulses from the pulse height counter were measured. The pulse height distribution for the total beam flux was determined in this manner and is plotted in Fig. 7 for each of the three energies. The peak in the pulse height spectrum is due to the pions in the beam. The full width at half maximum is about 20 percent and comes from a combination of a spread of about 10 percent in pion energy loss caused by the finite width of the pion energy distribution and a spread of 17 percent for the natural resolution of the pulse height counter, the latter being primarily due to statistical fluctuations in the number of photoelectrons collected in the photomultiplier tubes. In Fig. 7 the shift of the position of the peak with energy is proportional to the change in energy loss in the pulse height crystal with energy.

Although the introduction of the collimating counter reduced the minimum ionization background to a negligible amount, the pulse height resolution was sufficient to distinguish the pions from minimum ionization particles. The largest background was found in the large pulse region and was probably due to a proton flux or stars and knock-on protons from a random neutron background. It was well separated from the pion pulse height. The only background that could not be distinguished from the pions was that due to muons. Corrections for this

are discussed later. From the beam pulse height distribution, the fraction of the traces were determined for which the pulse height was inside the narrow pulse height band representing the pions. This was applied as a correction to the beam flux.

For every event that was found, the pulse height was measured. The pulse height distribution for the attenuation events is shown in Fig. 8 for the medium pion energy. The position and shape of the peak corresponds to that of the beam pulse height distribution. The additional pulses just above the main peak are due to muons that came from pion-muon decays ahead of the pulse height counter and that traveled through the crystals and ended their range in the attenuation target. This will be discussed in a later section. The same pulse height selection that was used for the beam flux was applied to the events. All events in which the pulse height fell outside of the narrow pion pulse height band were discarded. It should be mentioned that the beam pulse height distribution was determined by measurements on each of one or two oscilloscope traces that followed an event trace. In this way a random selection of traces was obtained and it could be verified that no drift or change in the pulse height distribution occured throughout a run.

2. Momentum Selection. In order to provide optimum use of the momentum selection provided by the target and exit slit geometry, runs were made with the production target removed. By this means it was possible to subtract out that portion of the flux and events not due to the presence of the production target. After pulse height selection, the flux with the production target removed was from 2 percent at the low energy to 4 percent at the high energy of the flux with the production target in place. Furthermore, the fractional number of pulse height selected events was the same under both conditions. It was presumed that most of the target-out particles with the pion pulse height were actually pions produced in the proton beam collimator walls and vacuum window. Since the actual effect of this target-out subtraction was nil, the subtraction was discontinued for the later runs. The combination of momentum selection and pulse height selection thus eliminated all background except for some of the muons arising from the decay of pions while in flight, which thus had to be treated by special methods.

3. The Attenuation Targets. To obtain the cross sections as a function of nuclear size, four elements were chosen for this study. They were beryllium, carbon, aluminum, and copper. Multiple coulomb scattering made the choice of materials of higher atomic number unfeasible. In Tables I and II the target thicknesses are listed. As previously mentioned, at the low energy it was necessary to reduce the thickness of the aluminum and copper targets for the second run to reduce the effects of multiple coulomb scattering. Except for this, at each energy the energy loss was the same in each target. The mean energies of the pions in the targets were 33, 46, and 68 Mev with an energy loss of 7 or 9.5, 10, and 11 Mev in the targets for the low, medium, and high energies respectively.

4. Calculation of the Cross Sections. From the total number of pulse height selected pions and the total number of pulse height selected events, the fraction of the pions causing events was calculated. Runs were made with the attenuation target in and with the attenuation target removed. A subtraction gave the fraction of the pions causing events in the target. After correction for muon flux, accidentals, false events due to pion-muon decay, and multiple coulomb scattering, as described below, the attenuation cross section per target nucleus and the ring counter cross section per target nucleus were computed using the equation

$$f = e^{-N\sigma x}, \qquad (1)$$

where f is the fraction of events, N the number of target nuclei per gram, σ the cross section in cm^2, and x the thickness of the target in grams/cm^2.

C. Corrections

1. Accidentals. The number of accidental sweeps was small and the number not obviously accidentals as determined by the increased time resolution afforded by measurements of the pulse separation on the projected trace image was negligible. As can be seen in Fig. 6, accidental single pulses appeared on the oscilloscope traces fairly frequently. If an accidental pulse had appeared at the position of the second or third pulse in the case of an event, these events would have been missed.

Consequently, the accidental pulse frequency was determined for each section of film and a small correction made to account for events missed because of this effect.

A more serious problem was the possibility of an accidental appearing at the position of the third pulse in the case of a particle passing undeviated through the counter system. This could be misinterpreted as a ring counter event unless a satisfactory pulse height selection was made on the second the third pulses. From a knowledge of the normal pulse height distribution for the inside section and for the ring section of the back counter and from a measurement of the pulse height distribution and frequency of the accidental pulses, a pulse height criterion for a ring counter event could be established with a maximum set for the pulse from the inside section and a minimum set for the ring section pulse. In this way the number of accidental ring counter events was reduced to a small correction. Accidentals were studied on the film for each target and energy and corrections were made as shown in Tables I and II.

2. Pion-Muon Decay. Nature has endowed the pion with an inconvenient lifetime. If it were shorter, the present experiment would not have been feasible. If it were longer, there would have been no problem. As it is, pion decay was rather troublesome. The presence of muons in the beam, due to the decay of pions while in flight, required a correction to both the flux and to the number of events. The muons from decay in flight were carried forward from the point of decay, by the center of mass motion, within a narrow cone with the maximum decay angle depending upon the pion energy. The laboratory energy of the muons varied between wide limits. For example, for 53 Mev pions the muon energy spectrum went from 17 Mev, corresponding to decay in the backwards direction in the center of mass, to 73 Mev, corresponding to decay in the forwards direction in the center of mass. Where the decay occured before the pulse height crystal and passed through the counter system, some of the low energy muons could be distinguished from the pion beam by the pulse height selection. Because of the solid angles involved, the important contributions to the muon flux through the attenuation target came from decays immediately before the pulse height counter and between the pulse height counter and the target.

The wide energy distribution of this muon flux was reflected in a wide range distribution such that most of the muons had considerably greater range than the pions. Consequently, to measure the muon flux, sufficient copper absorber was used to stop all of the pions and the number of long range particles having the pion pulse height was determined. It was assumed that these were muons and a suitable correction was made for those which were missed by this method. Thus it was found that about 4 percent of the pulse height selected flux through the attenuation target was due to muons. This could also be calculated on the basis of the counter geometry and the pion-muon decay kinematics and mean lifetime. The calculation failed to explain all of the long range particles observed and it was presumed that the extra particles were muons coming from the region of high pion density near the production target. These muons would have been fairly well selected in momentum and thus would have had sufficient range to be included in the measurement just described. It was assumed that the muons did not interact in the target and a 4 percent correction was made to the beam flux.

A far more serious problem came from the presence of muons having such low energy that they came to the end of their range in the attenuation target. Such an occurrence would appear as an attenuation event, since pulses from the back counter would be missing, except in those rare cases where a muon-positron decay occured within a small fraction of a microsecond and the positron passed through the back counter. If the low energy muon in question came from a pion decay ahead of the pulse height counter, the pulse height of the stopped muon would be sufficiently greater than that of the pions and the event would be rejected in the pulse height selection. These events are found in the excess of large pulses just above the pion pulse height peak in the attenuation event pulse height distribution of Fig. 8. The number and pulse height agrees well with the calculated value. However, for the stopped muons from pion decays between the pulse height counter and the attenuation target, one was left with no recourse but to derive a correction analytically. This was readily done from the knowledge of the geometry, of the stopping power of the counters and targets, and of the pion-muon decay lifetime and kinematics. These corrections are shown in Table I. The correction was largest at the low energy for beryllium and carbon. There was a smaller energy loss in the aluminum and copper targets at the low energy measurement and the correction was correspondingly less.

The problem was similar in the case of the ring counter events. Muons near the maximum laboratory decay angle could pass through the ring counter if the decay occured behind the pulse height counter. This would be recorded as a ring counter scattering event. To make this correction a graphical analysis was made in which the volume behind the pulse height counter through which the pion beam passed was divided up into small elements. For the muons decaying at each position and pion energy, an angular probability distribution was calculated from the pion-muon decay kinematics. The muons were sharply peaked at the maximum decay angle that was 25° for the lowest pion energy and slowly decreased with increasing energy. This maximum decay angle was generally just inside or outside the inner boundary of the ring counter and it was therefore necessary to take into account the multiple coulomb scattering of the pions and muons in the crystals and target. The multiple coulomb scattering gave rise to a small angular spread of the initial large angle muon decay. Thus the ring counter boundary for any given azimuthal decay angle was approximated by a tangent line to the actual circular boundary. By assuming the multiple coulomb scattering to be gaussian in the polar angle about the muon decay direction with a root-mean-square deviation as given in the next section, the probability distribution of scattering into any line parallel to the line tangent to the ring boundary could be calculated. This is simply the problem of multiple coulomb scattering into a plane which passes through the scattering point at a given angle to the polar direction. This probability distribution was folded into the angular distribution for the muons decaying at the beam volume element under consideration.

To account for the finite extent of the pion beam, the above result was folded into ring counter angular efficiency curves similar to those in Fig. 4. When integrated over angle, this gave the probability at each volume element that a muon would pass through the ring counter. This was multiplied by the fraction of pions decaying in the volume element and was summed over the contributing beam volume. That some of the muons from decays between the two front counters failed to travel through the passing counter was taken into account. This procedure resulted in the total fraction of the pion flux giving rise to false ring counter events due to pion-muon decay. These calculations were made at each energy

for each target and for the case with the target removed. The target-in, target-out subtraction was made and appears as the muon decay correction in Table II.

The correction can be traced to three effects: first, the increased multiple coulomb scattering with the target in; second, the stopping in the target of some muons that would otherwide reach the ring counter; and third, the decreased energy of pions after passing through the target and the subsequent increase in maximum pion-muon decay angle. It is to be noted that at the low energy and for aluminum and copper at the medium energy the correction was comparable to the statistical uncertainty of the measured ring counter event fractions. The muon decay correction was based upon three things: pion-muon decay kinematics and lifetime, geometry and stopping power, and multiple coulomb scattering. The first two were sufficiently well known and the effect of multiple coulomb scattering depended principally upon the width of the distribution rather than its detailed shape. It is believed that the treatment of the muon decay correction for both the ring counter events and the attenuation events was sufficient to make the uncertainty of the correction small compared to the statistical uncertainty of the measurements.

3. Multiple Coulomb Scattering. While ideally a "good" geometry is desired in an attenuation type experiment, "poor" geometry is required for the multiple coulomb scattering where charged particles are being studied. Consequently, the geometry used in the present experiment might be described as "mediocre". Compared to the effects being measured, multiple coulomb scattering is extremely large at the forward angles. It presumably falls off with angle like a gaussian and the multiple coulomb scattering was calculated by assuming a gaussian distribution in scattering angle with the mean square scattering angle given by

$$\overline{\theta^2} = bZ\,(\Delta E)/pc, \qquad (2)$$

where pc is the pion momentum in Mev, ΔE is the pion energy loss in Mev, Z is the atomic number of the scattering material, and b is a slowly varying function of Z and kinetic energy. For this experiment the values

of b were between 1.04 and 1.20. This formula was obtained by combining the dE/dx formula with the mean square scattering angle formula in a text by Fermi[11] with the scattering formula modified by setting the minimum impact parameter equal to the radius of the nuclei of the scattering material. For the thick targets used in the present experiment, Eq. (2) was integrated over the energy loss of the pions in the targets.

Based on calculations of multiple coulomb scattering at the low energy, where this effect was greatest, the target thicknesses and geometry were chosen to provide a managable correction for all but copper at the low energy, the latter being used to check emperically the multiple coulomb scattering correction. For the second run, for the case of aluminum and copper at the low energy, the target thickness was decreased and the angle subtended by the back counter was increased. The multiple coulomb scattering corrections were completely negligible in the case of the attenuation cross sections. For the ring counter cross sections the multiple coulomb scattering corrections are listed in Table II.

That the low energy copper cross sections agreed to within statistics is considered a verification of the multiple coulomb scattering correction to about 15 percent in this particular case. Consequently, the uncertainty in the correction for the second run for the low energy copper was considered to be small compared to the statistical uncertainty. However, at the medium energy, the correction for copper is seen to be much too large since it gives rise to a large negative cross section. In the analysis that is to be described later, it was found that the correction should be reduced by a factor of about ten to obtain internal consistency between the copper results and the medium energy cross sections for beryllium, carbon, and aluminum. No reasonable explanation has been found for this large discrepancy. Consequently, all cross sections for which the multiple coulomb scattering correction was comparable to or greater than the statistical uncertainty were not used for the analysis in the later sections. The cross sections that were discarded were those for the first run on the low energy aluminum and for copper at all energies except for the second run at low energy, where the multiple coulomb scattering correction was considered to be emperically verified.

IV THE MEASURED CROSS SECTIONS

In Table I the measured attenuation cross sections are given as well as the data and corrections pertinent to them. In the first column are the mean energies of the pion beams in the targets with the spread caused by the energy width of the beam and the energy loss in the targets. The second column gives the half angle, α_2, subtended by the full back counter as shown in Fig. 3. In the next column are listed the target nuclei. The fourth column gives the dimensionless quantity, kR. k is the wave number of the incident pion and R is the radius of the nucleus. In the next column the measured fraction of pions attenuated from the beam by the target is given. The uncertainty listed is the standard deviation due to the statistics of counting. The next two columns show the accidental and muon decay corrections as described in the previous section. The correction for multiple coulomb scattering was negligible. The column headed $\sigma_m/\pi R^2$ gives the resulting measured cross section divided by nuclear area. Nuclear area was taken to be πR^2, where $R = r_o A^{1/3}$. A is the mass number and $r_o = \hbar/m_\pi c = 1.4 \times 10^{-13}$ cm.

For the analysis that follows it was desired to remove the effects due to coulomb suppression of the positively charged pion wave function at the nucleus. This correction was derived in the following way. The classical particle picture was used for coulomb scattering to determine the impact parameter for a pion passing at a minimum distance R from the center of the nucleus. This impact parameter was called b_N and the cross section divided by the effective nuclear area was written as $\sigma_m/\pi b_N^2$. In the classical coulomb scattering, $b_N^2 = R^2/(1 + V_c/T_\pi)$, where T_π is the kinetic energy of the pion and V_c is the coulomb barrier, i.e., the coulomb potential at the radius R. Consequently, the cross section divided by nuclear area, when corrected for coulomb suppression of the pion wave function at the nucleus, was taken to be $(\sigma_m/\pi R^2)(1 + V_c/T_\pi)$. The corrections and the corrected cross sections are listed in the last two columns of Table I.

Similar information is listed for the ring counter cross sections in Table II. Two additional columns are for the half angle subtended by the inside ring boundary of the back counter, α_1, and for the multiple coulomb scattering correction. The measured ring counter cross section

is called $\Delta \sigma_m$. Except for the cases marked with an asterisk, the systematic errors were estimated to be small compared to the statistical uncertainties shown for both the ring counter and attenuation cross sections.

TABLE I

Measurements of the Attenuation Cross Sections

Pion Energy	α_2	Target	kR	Target Thickness gm/cm^2	Measured Fraction of Pions Attenuated Times 100	Correction Fractions Times 100		$\sigma_m/\pi R^2$	$1 + V_c/T_\pi$	$\sigma_m(1+\frac{V_c}{T_\pi})/\pi R^2$
						Acci-dentals	Muon-decay			
33±6	35°	Be	1.50	2.587	1.88±0.20	+0.07	-0.27	0.366±0.044	1.058	0.387±0.047
33±6	35	C	1.65	2.555	1.84±0.21	+0.07	-0.30	0.389±0.050	1.079	0.420±0.054
33±5	42	Al	2.16	2.012	1.25±0.19	+0.07	-0.21	0.456±0.088	1.131	0.515±0.099
33±5	42	Cu	2.88	2.342	1.20±0.19	+0.07	-0.21	0.486±0.090	1.220	0.593±0.105
46±6	35	Be	1.80	3.452	2.93±0.27	+0.07	-0.14	0.473±0.044	1.042	0.492±0.046
46±6	35	C	2.00	3.232	3.05±0.27	+0.08	-0.17	0.570±0.052	1.057	0.603±0.055
46±6	35	Al	2.60	3.826	3.21±0.28	+0.07	-0.17	0.666±0.058	1.094	0.730±0.064
46±6	35	Cu	3.47	4.224	2.45±0.25	+0.08	-0.17	0.606±0.064	1.158	0.702±0.074
68±10	35	Be	2.27	4.601	5.28±0.32	+0.19	-0.01	0.684±0.041	1.028	0.703±0.042
68±10	35	C	2.50	4.190	4.46±0.30	+0.17	-0.01	0.695±0.046	1.038	0.722±0.048
68±10	35	Al	3.28	4.748	4.75±0.32	+0.16	-0.02	0.840±0.055	1.064	0.903±0.059
68±10	35	Cu	4.37	5.620	4.20±0.31	+0.15	-0.02	0.847±0.061	1.107	0.938±0.068

TABLE II

Measurements of the Ring Counter Cross Sections

Pion Energy	α_1	α_2	Target	kR	Target Thickness gm/cm^2	Measured Ring Counter Fractions of Pions Times 100	Correction Fraction Times 100: Accidentals	Muon decay	Mult. coul. Scat.	$\Delta\sigma_m/\pi R^2$	$1+V_c/T_\pi$	$\Delta\sigma_m/(1+V_c/T_\pi)/\pi R^2$
33±6	21.7°	35°	Be	1.50	2.587	0.32±0.14	-0.03	-0.14	-0.00	0.031±0.030	1.058	0.032±0.031
33±6	21.7	35	C	1.65	2.555	0.55±0.15	-0.03	-0.18	-0.02	0.074±0.034	1.079	0.081±0.037
33±6	21.7	35	Al	2.16	2.704	1.13±0.25	-0.01	-0.23	-0.41	0.137±0.071	1.131	0.155±0.080*
33±5	26.6	42	Al	2.16	2.012	0.40±0.13	-0.03	-0.14	-0.00	0.085±0.045	1.131	0.096±0.051
33±6	21.7	35	Cu	2.88	3.242	4.90±0.60	-0.01	-0.29	-4.42	0.038±0.165	1.220	0.046±0.201*
33±5	26.6	42	Cu	2.88	2.342	0.91±0.16	-0.06	-0.22	-0.40	0.090±0.060	1.220	0.110±0.073
46±6	21.7	35	Be	1.80	3.452	0.27±0.13	-0.03	-0.06	-0.00	0.027±0.021	1.042	0.028±0.022
46±6	21.7	35	C	2.00	3.232	0.45±0.15	-0.03	-0.09	-0.00	0.061±0.026	1.057	0.065±0.028
46±6	21.7	35	Al	2.60	3.826	1.02±0.18	-0.03	-0.20	-0.08	0.148±0.034	1.094	0.161±0.037
46±6	21.7	35	Cu	3.47	4.224	1.24±0.17	-0.03	-0.30	-1.66	(-0.23±0.05)	1.158	--------- *
68±10	21.7	35	Be	2.27	4.601	0.65±0.17	-0.07	-0.00	-0.00	0.071±0.020	1.028	0.073±0.021
68±10	21.7	35	C	2.50	4.190	0.64±0.18	-0.06	-0.00	-0.00	0.084±0.026	1.038	0.087±0.026
68±10	21.7	35	Al	3.28	4.748	0.92±0.18	-0.06	-0.00	-0.00	0.146±0.029	1.064	0.155±0.031
68±10	21.7	35	Cu	4.37	5.620	1.04±0.18	-0.06	-0.00	-0.36	0.105±0.020	1.107	0.116±0.035*

* Omitted from analysis due to uncertainty in multiple coulomb scattering correction.

V THE COMPLEX SQUARE WELL MODEL

A. General Description

The pion-nucleus cross section may be considered to consist of two parts, an elastic cross section, σ_s, that is the coherent scattering by the nucleus as a whole, and an interaction cross section, σ_a, that includes all other processes such as absorption or star formation, inelastic or noncoherent scattering, and charge exchange scattering. Thus the measured attenuation cross section included all of σ_a except for a small fraction for cases in which an ionizing particle from the interaction passes through the back counter. It also included all elastic scattering for angles greater than α_2. Thus the measured attenuation cross section may be written as

$$\sigma_m = F_a \sigma_a + F_{\alpha_2} \sigma_s \tag{3}$$

where F_a is the fraction of the interaction cross section included in the measurement and F_{α_2} is the fraction of the total elastic scattering cross section for angles greater than α_2.

The ring counter cross section included primarily the elastic scattering for angles between α_1 and α_2 and a small contribution due to ionizing particles from an interaction event. Single coulomb scattering also contributed to the ring counter cross section, as did the interference between the nuclear and the coulomb scattering. The measured ring counter cross section may therefore be written as

$$\Delta\sigma_m = \Delta F_a \sigma_a + \Delta F_\alpha \sigma_s + \Delta\sigma_{coul.} + \Delta\sigma_{interf.}, \tag{4}$$

where ΔF_a and ΔF_α are the fraction of interaction and scattering events reaching the ring counter.

Because of the "mediocre" geometry, the measured cross sections were a mixture of the above types of cross sections and the measured cross sections were impossible to interpret by themselves. Consequently, a model was required for the analysis of the various components of the cross sections. The coulomb scattering and coulomb interference were treated in the Born approximation and will be described later. For the nuclear part, a model was chosen in which the interaction is represented by a complex square well, $V_r + iV_i$, of radius $R = r_o A^{1/3}$, where r_o =

$\hbar/m_\pi c = 1.4 \times 10^{-13}$ cm. A plane wave amplitude outside the square well may be written with the spacial dependence e^{ikx}, where $k = p_\pi/\hbar$ is the outside wave number and p_π is the initial pion momentum. Inside the square well the plane wave amplitude may be written as $e^{ik'x}$, where

$$k' = k + k_1 + ik_2 = p_\pi'/\hbar \tag{5}$$

is the inside wave number. Here p_π' is the complex momentum of the pion inside the square well. Although the analysis was implicity based on the Schroedinger wave equation, relativistic momenta were used throughout in deriving the wave numbers. k_1 is the difference between the real part of the inside wave number and the outside wave number. k_2 is the imaginary part of the inside wave number.

The amplitude of a plane wave inside the square well contains the term $e^{-k_2 x}$ which represents a decrease in amplitude. This is interpreted as the removal of pions from the coherent wave and k_2 may be expected to be directly related to the interaction cross section, σ_a. The coherent scattering cross section, σ_s, is strictly a wave phenomenon and will depend upon both k_1 and k_2. Hereafter, k_1 and k_2 will be considered as the parameters of the analysis rather than the complex square well itself. The problem was to find a unique pair of parameters k_1 and k_2, at each pion energy, that would fit both the measured attenuation and ring counter cross sections and to evaluate the effect of the statistical uncertainty of the measurements in this choice.

B. The Optical Model

An exact solution for the cross sections σ_a and σ_s may be obtained for the complex square well by means of a partial wave analysis.[12] However, calculation of the phase shifts as a function of k and R for the two arbitrary parameters k_1 and k_2 was found to be excessively time consuming and was beyond the scope of this paper. Consequently, the approximate derivation of σ_a and σ_s by the optical model of Fernbach, Serber, and Taylor[13] was used. The approximation in the optical model is the neglecting of reflection and refraction of the incident wave at the boundary of the square well. The cross sections as derived in the optical model are

$$\sigma_a/\pi R^2 = 1 - \left[1 - (1 + 4k_2R)\, e^{-4k_2R}\right]/8k_2^2R^2$$

$$\sigma_s/\pi R^2 = 1 + \left[1 - (1 + 4k_2R)\, e^{-4k_2R}\right]/8k_2^2R^2 \tag{6}$$

$$- \left[1/(k_2^2R^2 + k_1^2R^2)^2\right] \Big\{(k_2^2R^2 - k_1^2R^2)$$

$$+ e^{-2k_2R}\left[2k_1R\,(k_2^2R^2 + k_1^2R^2) + k_2Rk_1R\right] \sin 2k_1R$$

$$- e^{-2k_2R}\left[(k_2^2R^2 - k_1^2R^2) + 2k_2R\,(k_2^2R^2 + k_1^2R^2)\right] \tag{7}$$

$$\cos 2k_1R\Big\}.$$

k_2 is the parameter $K/2$ in reference 13.

The angular distribution in reference 13 is given as

$$f(\theta) = k/2 \sum_{\ell=0}^{\ell+\frac{1}{2}<kR} (2\ell+1)\left[1 - e^{\left\{(-2k_2R+2ik_1R)\left[k^2R^2-(\ell+\frac{1}{2})^2\right]^{1/2}/kR\right\}}\right] P_\ell(\cos\theta). \tag{8}$$

From this, there could be derived the fraction scattered at angles greater than α_2, $F\alpha_2$, and the fraction scattered into the ring counter, ΔF_α. This was done for several different pairs of parameters, k_1R and k_2R, with the result that these fractions were found to be independent of k_1R and k_2R and were a function only of kR. This seems reasonable, since the angular distribution depends upon the number of orders of partial waves present which in turn depends only upon the relation between the size of the square well and the wave number of the incident wave.

F_{α_2} and ΔF_α are shown as a function of kR in Fig. 9 for the two choices of α_1 and α_2 used in the present experiment. In the limit of zero kR the scattering is isotropic. As kR is increased, i.e., as the radius of the square well is increased with respect to the wave length of the incident wave, the scattering takes on the nature of a forward-peaking diffraction scattering. The fraction scattered at angles greater than α_2, F_{α_2}, decreases as the diffraction scattering is carried more into the forward direction with increasing kR. The fraction scattered into the interval from α_1 to α_2, ΔF_α, increases as the diffraction scattering becomes more peaked in the forward direction with increasing kR. It then drops at very large kR as the diffraction scattering comes almost entirely within the angle α_1.

C. Coulomb Scattering

The coulomb scattering and the coulomb interference were calculated by means of the Born approximation. In terms of wave numbers, the Born approximation for the scattering amplitude for a spherical potential can be written as

$$f(\theta) = \int_0^\infty \frac{\sin \eta}{\eta} (k'^2 - k^2)\, r^2\, dr, \tag{9}$$

where k is the wave number of the incident wave, k' is the wave number at the distance r from the center of the scattering potential, and $\eta = 2kr \sin(\theta/2)$. Again relativistic wave numbers were used so that

$$k'^2 - k^2 = (p'^2 - p^2)/\hbar^2 = -V(-V + 2E)/\hbar^2 c^2, \tag{10}$$

where V is the potential at r and E is the relativistic total energy. With this treatment, the example of the small angle coulomb scattering from a point charge becomes relativistically correct and it was thus considered an improvement over the nonrelativistic case.

For the present use, the potential was taken to be the screened coulomb potential of a uniformly charged sphere of radius R and charge Ze in addition to the complex square well $V_r + iV_i$, also of radius R:

$$\begin{aligned} V &= (Ze^2/R)(r^2/R^2) + V_r + iV_i, \quad r < R, \\ &= (Ze^2/R/r)\, e^{-r/a_o} \qquad\qquad , \quad r > R. \end{aligned} \tag{11}$$

After the integration as indicated in Eq. (9), the coulomb scattering amplitude becomes, except for negligible cross terms,

$$f_C(\theta) = -(6Ze^2\, ER^2/\hbar^2 c^2)\left[\eta^2 \sin \eta - 2(\sin \eta - \eta \cos \eta)\right]/\eta^5, \tag{12}$$

where Eq. (10) has been used. The contribution from the complex square well is

$$f_V(\theta) = \left[(k + k_1 + ik_2)^2 - k^2\right] R^3 (\sin \eta - \eta \cos \eta)/\eta^3, \tag{13}$$

where Eqs. (5) and (10) may be used to relate the parameters k_1 and k_2 to the complex square well $V_r + iV_i$.

It was found that the angular distribution of $f_V(\theta)^2$ was the same as the angular distribution for scattering in the optical model. However, the magnitude of the scattering was larger for the Born approximation than for the optical model. For small k_1R and k_2R, the two models gave equal scattering, but if either parameter became large, that is, when there was appreciable disturbance of the incident wave, the discrepancy between the Born approximation and optical model increased. Consequently, $f_V(\theta)$ was renormalized in magnitude for each pair of k_1R and k_2R to agree with the optical model. Since angular distributions due to the complex square well were the same for the two models, it was believed that the interference term derived from the renormalized Born approximation was satisfactory.

From the differential scattering cross section, $d\sigma/d\Omega = |f_C + f_V|^2$, the contribution to the ring counter cross section due to coulomb scattering and coulomb interference was calculated by integrating f_C^2 for the coulomb scattering, and $2f_C$ times the real part of f_V for the interference, over the solid angle from the inside boundary of the ring counter, α_1, to the outside boundary, α_2. The sign of the interference contribution was taken to be negative on the basis of the cloud chamber experiment of Byfield, et al,[5] in which the elastic scattering angular distribution of 62 Mev positive pions on carbon was found to have a pronounced dip for small angle scattering. This was interpreted by them as indicating that the real part of the square well was attractive. Consequently, for the present experiment, the coulomb interference was considered to be destructive and was subtracted from the pure coulomb and nuclear contributions.

D. Star Prong Correction

There remains the question of what to use for F_a and ΔF_a in Eqs. (3) and (4). The nuclear emulsion[1,2,3] and cloud chamber experiments[4,5] indicate that most of the interaction cross section is due to star formation. Consequently, the star prong frequency and energy distributions of Bernardini and Levy[3] for star prongs from π^+ in nuclear emulsions were used for these calculations. Most of the protons emerging

from a star interaction were of such low energy that they could not penetrate the remainder of the target and pass through the aluminum foil on the face of the back counter. Consequently, at several depths through the target, the number of protons per star capable of reaching the back counter was calculated, based upon the energy and frequency distribution of star prongs in nuclear emulsions. This was averaged through the target and it was found that about one ionizing prong per star was capable of reaching the back counter.

Assuming isotropy of these star prongs, it was found that about 9 percent for $\alpha_2 = 35^o$ and 13 percent for $\alpha_2 = 42^o$ of the interaction cross section was lost in the measurement of the attenuation cross section because of star prongs reaching the back counter. Consequently, F_a was taken to be 0.91 and 0.87 for the two geometries. Similarly, for the ring counter cross sections, ΔF_a was found to be 0.055 for the smaller angle geometry and 0.073 for the larger angle geometry. These calculations are subject to serious question, particularly with respect to the energy dependence and dependence upon nuclear size of the star prong energy distributions. However, the relative contribution of this effect was small.

E. Determination of the Inside Wave Numbers

To compare with the measured cross sections, σ_m and $\Delta\sigma_m$ were computed according to Eqs. (3) and (4). For each target nucleus and pion energy, curves were plotted of σ_m and $\Delta\sigma_m$ versus either one of $k_1 r_o$ or $k_2 r_o$ and for several values of the other parameter. For a given energy one parameter was then arbitrarily chosen and the second parameter was determined to give the correct measured attenuation cross section, σ_m, for each element at this energy. The second parameter was also assigned an uncertainty derived directly from the standard deviation of the measurement. The values of the second parameter for the several target elements were combined in the optimum statistical manner. This procedure was repeated for a number of choices of the first parameter giving a set of pairs of the parameters for best fits to the several measurements of σ_m at the given energy. Thus a curve could be plotted of $k_1 r_o$ versus $k_2 r_o$ such that for an arbitrary choice of one parameter, the curve determined the second

parameter for a best fit to the measured cross sections. This was repeated at the other two pion energies. Figs. 10, 11, and 12 show the pairs of the parameters as determined by the measured attenuation cross sections, σ_m, at 33, 46, and 68 Mev. The dashed lines indicate the uncertainty limits as derived from the standard deviations of the individual measurements and combined in the optimum statistical manner.

This analysis was also carried out for the measured ring counter cross sections, $\Delta\sigma_m$. Again, curves were plotted for pairs of parameters, k_1r_o and k_2r_o, that gave best fits to the ring counter data. These are also shown for the three energies in Figs. 10, 11, and 12 with the uncertainty limits as derived from the statistical uncertainties. It should be noted that the uncertainty limits no longer represent standard deviations in the true statistical sense, due to the nonlinearity in the dependence of the cross sections on the parameters. However, they are retained to indicate the sensitivity of the determination of the parameters to the statistical uncertainty of the data.

In Figs. 10, 11, and 12 the intersections of the curves from the attenuation cross sections with the curves from the ring counter cross sections give the pairs of parameters for the best fit to both cross sections at the three energies. These are shown in Table III.

TABLE III

Parameters for the Best Fit to the Measured Cross Sections

T_π	k_1r_o	k_2r_o
33 Mev	$0.18^{+0.03}_{-0.04}$	$0.04^{+0.03}_{-0.02}$
46	$0.26^{+0.03}_{-0.05}$	$0.03^{+0.04}_{-0.03}$
68	$0.17^{+0.05}_{-0.13}$	$0.17^{+0.05}_{-0.04}$

The uncertainties listed are approximately determined by the crossovers of the uncertainty limits in Figs. 10, 11, and 12.

For the above best-fit values of the parameters, attenuation cross sections as calculated according to Eq. (3) are plotted versus kR

in Figs. 13, 14, and 15 for the three pion energies. Also shown are the measured cross sections corrected by the factor $1 + V_c/T_\pi$. It is seen that while the total cross section continues to rise with increasing kR, the "mediocre" geometry attenuation cross section rises at first, levels off, and approaches the interaction cross section with increasing kR. This is readily understood in terms of the forward peaking of the diffraction scattering as kR is increased.

For the same parameters the ring counter cross sections, as calculated according to Eq. (4), are plotted in Figs. 16, 17, and 18. The contributions due to square well scattering, coulomb scattering, and coulomb interference are also shown, as is the star prong estimate. The measured ring counter cross sections, corrected by the factor $1 + V_c/T_\pi$, are also plotted in Figs. 16, 17, and 18. As previously mentioned, the uncertainty in the multiple coulomb scattering correction required the omission of the copper cross sections at 46 and 68 Mev as well as the results from the first run on aluminum and copper at 33 Mev. The geometry for beryllium and carbon at the low energy was different from that for the aluminum and copper points in Fig. 16 and they are not shown. The beryllium and carbon cross sections at 33 Mev were given negligible statistical weight and contributed little to the determination of the best-fit parameters. They are, however, internally consistent with the final choice of parameters at this energy. In general, the rapid rise in the calculated ring counter cross sections with increasing kR caused the measured points of greater kR to have a considerably larger statistical weight in the parameter analysis than points of lower kR. Internal consistency for both the attenuation and the ring counter cross sections is seen to be satisfactory.

F. Energy Dependence of the Interaction Parameter and the Interaction Cross Sections

Of particular significance is the energy dependence of $k_2 r_o$. The exponential decrease of a pion plane wave probability is $e^{-2k_2 x}$. By considering the complex square well to be composed of an aggregate of interaction centers represented by the nucleons in the nucleus, this exponential decrease may be written as $e^{-N\sigma_n x}$, where N is the nucleon density and σ_n is the cross section for the interaction of a pion with

a bound nucleon in the nucleus. For free nucleons, the total pion cross section is found for pion energies of interest here[14] to emperically satisfy an energy dependence given by p_π^4/E_π^2, where p_π is the pion momentum and E_π is the total relativistic energy. This energy dependence is simply the result of a second order gradient coupling theory for the pion-nucleon interaction.

While the presence of other nucleons in the nucleus complicates the theoretical picture tremendously, one may ignore, as a first approximation, the effects of neighboring nucleons upon a given nucleon. With this simplifying assumption, one may consider the interaction cross section for a bound nucleon to be proportional to p_π^4/E_π^2. Consequently, one may write

$$k_2 r_o = b(kr_o)^4/\gamma^2, \tag{14}$$

which is the p_π^4/E_π^2 energy dependence, since $k = p_\pi/\hbar$ and $\gamma = E_\pi/R_\pi$, where R_π is the rest energy of the pion. b is considered a constant. The values of $k_2 r_o$ determined by the present experiment are plotted in Fig. 19 as a function of pion energy. The curve representing Eq. (14) is also shown with b determined to be $0.21^{+0.04}_{-0.03}$ by a least squares fit. It is seen that the measured values are fairly consistent with the strong energy dependence given by Eq. (14) although the poor statistics do not allow a detailed comparison.

The empirical validity of Eq. (14) may be further tested by an examination of the published results for the interaction cross section, σ_a, from other experiments. There have been several experiments in which the carbon nucleus has been used as a target. For the cloud chamber experiments[4, 5] the published cross sections for stars, stops, and inelastic scattering were added to give σ_a. These were divided by πR^2 and multiplied by $1 \pm V_c/T_\pi$ to approximately remove the coulomb effect. The positive and negative signs are for positive and negative pions respectively. Similarly, the cross sections of Martin[6] were multiplied by $(1 - V_c/T_\pi)$. The results are plotted in Fig. 20 as a function of the dimensionless parameter kR. The carbon interaction cross sections, as determined in the present experiment by the optical model analysis with the values of $k_2 r_o$ in Table III, are also shown. These

were compared with the interaction cross section, σ_a, as calculated from the optical model as represented by Eq. (6), with the energy dependence for $k_2 r_o$ as given by Eq. (14). A least squares fit using all the plotted data was made giving for the best value of b in Eq. (14) 0.26 ± 0.03.

The sharp drop of the nuclear emulsion cross sections with decreasing energy is also explained by Eq. (14). The published results for the cross sections for stars, stops, and inelastic scatters in nuclear emulsions[1,2,3] were added to give σ_a. This was divided by the weighted average for πR^2 for nuclear emulsion given by Bradner, et al[3] and multiplied by $1 \pm V_c/T_\pi$. These are plotted versus kR in Fig. 21. A least squares fit gave $b = 0.24 \pm 0.04$ for the positive pion data and $b = 0.36 \pm 0.07$ for the negative pion data. The resulting curves for the interaction cross sections are also shown in Fig. 21.

G. Mean Free Path for Interaction in Nuclear Matter

The data from the present experiment and from other experiments may be treated in still another way. Writing $e^{-2k_2 x} = e^{-x/\lambda_a}$, one may interpret λ_a as the mean free path for interaction of pions in nuclear matter, where

$$\lambda_a = (2k_2)^{-1}. \tag{15}$$

From the values of $k_2 r_o$ determined by the present experiment and analysis at 33, 46, and 68 Mev pion energies, the mean free path in units of r_o, λ_a/r_o, can be calculated. Similarly, by deriving the quantity $\sigma_a (1 \pm V_c/T_\pi)/\pi R^2$ from the published data of the other experiments listed above, it is possible to determine the values of $k_2 r_o$ at several other energies by means of the optical model analysis as represented by Eq. (6). Then, by using Eq. (15), the values for the mean free path for interaction in nuclear matter may be calculated. The various results for λ_a/r_o are given in Fig. 22 plotted against pion kinetic energy. This is to be compared with the energy dependence of λ_a/r_o as given by Eqs. (14) and (15). The result for a least squares fit to all plotted points is shown in Fig. 22. The value of b in Eq. (14) giving the best fit is $b = 0.262 \pm 0.023$.

A summary for the various values of b determined by the optical model analysis and by various sources of data, as discussed above, is given in Table IV.

TABLE IV

Values of b from Least Squares Fit

Source	b from Eq. (14)
The present experiment (see Fig. 19)	$0.21 \begin{smallmatrix} +0.04 \\ -0.03 \end{smallmatrix}$
All carbon data (see Fig. 20)	0.26 ± 0.03
Nuclear emulsion data for π^+ (see Fig. 21)	0.24 ± 0.04
Nuclear emulsion data for π^- (see Fig. 21)	0.36 ± 0.07
All of the above data (see Fig. 22)	0.262 ± 0.023

H. Relation to the Interaction of Pions with Free Nucleons

It was previously assumed that the effect of a nucleon being bound in a nucleus had no effect upon the free nucleon p_π^4/E_π^2 energy dependence, and the normalization for this energy dependence was determined by the nucleus interaction cross section data. Satisfactory agreement with the results of this simplifying assumption was found. However, it is unnecessary to depend upon this oversimplification. The square well parameters may be determined by combining the interaction of pions with free nucleons with the multiple scattering theory in which the presence of neighboring nucleons is taken into account.

As presented by Lax[15] and applied to nuclei, the multiple scattering theory considers the nucleus to consist of an ensemble of interaction centers or scatterers representing the nucleons, the ensemble being described by a given probability distribution in space and quantum states. To determine the interaction of an incoming wave with this ensemble, the total wave is found and averaged adiabatically over the ensemble distribution. The case of a homogeneous medium (uniform spatial density) is considered and the equation

$$k'^2 - k^2 = 4\pi ncf(0^o) \tag{16}$$

is found to determine the magnitude of the propagation vector in the medium of the scatterers. k' and k are the inside and outside wave numbers, n is the density of scatterers given by $n = (4\pi r_o^3/3)^{-1}$, and c is a constant depending upon the correlation between pairs of scatterers. For the present application, c was taken to be unity. $f(0^o)$ is the forward scattering amplitude in the case for a free nucleon.

To calculate $f(0^o)$, phase shifts were used that were derived by Anderson, et al[16] from the angular distributions at 120 and 135 Mev for $\pi^+ \rightarrow \pi^+$, $\pi^- \rightarrow \pi^-$, and $\pi^- \rightarrow \pi^o$ with a liquid hydrogen target. Six phase shifts were derived. These are denoted by a^T_{LJ}, where T is the total isotopic spin, L is the total orbital angular momentum, and J is the total angular momentum. The six phase shifts were for T = 1/2, 3/2 and for angular momentum states $s_{1/2}$, $p_{1/2}$ and $p_{3/2}$. The scattering amplitude is derived by a transformation from the initial state described by quantum numbers (L, S, m_L, m_S) to the intermediate state described by quantum numbers (L, S, J, m_J) by means of the Clebsch-Gordan coefficient (L, S, m_L, m_S| L, S, J, m_J). This is followed by a transformation from the intermediate state to the final state described by quantum numbers (L, S, m_L, m_S) by means of the inverse Clebsch-Gordan coefficient. The coefficients are evaluated in Condon and Shortley.[17]

For the particular case of zero degrees, the scattering amplitudes for the three angular momentum states are

$$a^T_{s_{1/2}} = (e^{2i\,\delta^T_{s1/2}} - 1)/2\,ik,$$

$$a^T_{p_{1/2}} = -\,(e^{2i\,\delta^T_{p1/2}} - 1)/2\,ik,$$

$$a^T_{p_{3/2}} = e^{2i\,\delta^T_{p_{3/2}}} - 1)/\,ik.$$

For each isotopic spin state, the scattering amplitude is

$$a^T = \sum_{LJ} a^T_{LJ}$$

For convenience, spinar wave functions have been replaced by unity.

To determine the contribution of these scattering amplitudes to the individual types of pion-nucleon interactions the problem is considered in isotopic spin space under the assumption of conservation of total isotopic spin. A transformation is made from the initial state (τ_π, τ_N, m_{τ_π}, m_{τ_N}) through an intermediate state (τ_π, τ_N, T, m_T) to the final state (τ_π, τ_N, m_{τ_π}, m_{τ_N}) by means of the corresponding Clebsch-Gordan coefficients. Here, T is the total isotopic spin, τ_π is the pion isotopic spin, τ_N is the nucleon isotopic spin, and m refers to their projections. It should be noted that in contrast to the previous angular momentum problem, here the projections m_{τ_π} and m_{τ_N} retain their identity since these distinguish between positive, neutral, and negative pions and between protons and neutrons. The scattering amplitudes for each process are found to be

$$f(\pi^+ + p \rightarrow \pi^+ + p) = a^{3/2},$$

$$f(\pi^- + p \rightarrow \pi^- + p) = 1/3\,(a^{3/2} + 2a^{1/2}),$$

$$f(\pi^- + p \rightarrow \pi^o + n) = \frac{\sqrt{2}}{3}\,(a^{3/2} - a^{1/2}).$$

These were calculated from the phase shifts given by Anderson, et al.[16]

For the application to the multiple scattering problem represented by Eq. (16), the fact that the nucleus is composed of both protons and nucleons must be taken into account. Thus, in the case of positive pions, for example, one must write

$$f_{\pi^+}(0^o) = (Z/A)\, f_{\pi^+ + p}(0^o) + (N/A)\, f_{\pi^+ + n}(0^o),$$

where Z is the number of protons in the nucleus, N is the number of neutrons, and A = N + Z. For the present application Z was taken to be equal to N. $f_{\pi^+ + p}(0^o)$ was calculated as described above and $f_{\pi^+ + n}(0^o)$ was determined from

$$f_{\pi^+ + n}(0^o) = \pm f_{\pi^- + p}(0^o),$$

where the positive sign is taken for the pseudoscalar (PS) pion field and the

negative sign is taken for the pseudovector (PV) or scalar (S) pion field.[18] Since these scattering amplitudes are for the center of mass system of the pion and nucleon, the scattering amplitudes were transformed to the laboratory system for application to the multiple scattering in the nucleus. From this, the parameters $k_1 r_o$ and $k_2 r_o$ were calculated from Eqs. (16) and (5). The sign of the scattering amplitude was taken to be that corresponding to a repulsive square well. The mean free path for interaction in nuclear matter was then calculated by using Eq. (15). This was done for both the PS and PV or S cases.

Similar calculations were performed using the phase shifts determined by Bodansky et al[19] from the $\pi^+ + p$ angular distribution at 58 Mev. They assumed scattering through the T = 3/2 isotopic spin state only and thus have three phase shifts for the $s_{1/2}$, $p_{1/2}$, and $p_{3/2}$ angular momentum states. The signs of these phase shifts may be arbitrarily changed except for the coulomb interference. At 58 Mev, Bodansky et al,[19] find sufficient coulomb interference to give two different sets of phase shifts corresponding to positive and negative coulomb interference. The former is referred to by them as the case of positive $\alpha^{3/2}_{s_{1/2}}$ and the latter as the case of negative $\alpha^{3/2}_{s_{1/2}}$. While the latter is found by them to be statistically more probable, the former is not disallowed. Using their results for the two cases, λ_a/r_o was calculated for both PS and PV or S fields.

In Fig. 23 the values of λ_a/r_o calculated from the above phase shifts for the PS and PV or S cases are shown for 120 and 135 Mev and for the positive and negative $\alpha^{3/2}_{s_{1/2}}$ cases of Bodansky et al[19] at 58 Mev. Also shown is the curve giving the mean free path for the best fit for the pion-nucleus interaction. The points for the PV or S field are clearly much too high, pointing out the favorability of the PS pion field that is generally accepted today. No attempt was made to derive the statistical uncertainty for the plotted points, so it is difficult to tell whether the fact that the plotted points correspond to longer mean free paths than are derived for complex nuclei is due to a failing of the analysis or due to the statistical uncertainty present in the data. However, it is seen that the points derived from the interaction of pions with free nucleons do qualitatively follow the energy dependence found from the interaction of pions with complex nuclei.

VI DISCUSSION

Although the statistical uncertainties were rather large, expecially for the ring counter cross sections, the two inside wave number parameters could be adjusted to give internal consistency between the calculated cross sections and the seven or eight measured cross sections at each energy. This points out the usefulness of the optical model treatment of the complex square well interaction in interpreting the data. The strong energy dependence of the interaction suggested by the analysis of the data and shown in Fig. 19 was assumed to be the same as that for the free nucleon case. This assumption was emperically verified by a comparison with both the results of the present experiment and the results of other experiments.

That the optical model should provide a consistent picture of the pion-nucleus interaction over a wide range of energies may be at first surprising in view of the optical model assumption of no reflection or refraction at the square well boundary. However, two things reduce the error in using this assumption. First, one may expect that in reality the effective boundary of a nucleus is much less abrupt than the step function used for the square well. This should reduce the effect of reflection and refraction from that obtained in an exact solution to the square well problem. Secondly, for the case of the interaction cross section, the reduction of the wave amplitude passing through the nucleus due to reflection at the entrance boundary should to some extent counteract the increased path length inside the square well due refraction at the boundary. Consequently, the optical model may be applied with a fair degree of confidence.

It has been pointed out[5] that a wave analysis fails to explain the large amount of back-scattering found in the nuclear emulsion[1,2,3] and cloud chamber[4,5,20] experiments. The experiment of H. Heckman[21] is also pertinent. LeLevier has suggested[22] that a strong repulsive core to the nuclear potential would give rise to the back-scattering from the wave analysis. Peaslee[23] has attempted to explain these results by adopting an extreme single nucleon scattering model. While these back-scatterings are elastic within the rather broad uncertainty of the energy measurements, they may, however, be incoherent scatters in

which the pion interacts with a single nucleon rather than the nucleus as a whole. If so, the large back-scattering is expected from the results of Anderson, et al,[16] and of Bodansky, et al.[19] In terms of the analysis considered in the present experiment, such events would be included in the interaction cross section, σ_a, rather than the coherent scattering cross section, σ_s.

It is seen from Figs. 20 and 21 that at the highest energies the interaction cross sections are somewhat larger than the curves would predict. However, for the strong interactions found at the high energies, the cross section, which approaches nuclear area, is quite insensitive to the interaction parameter. Cross section measurements in this case serve only to define an upper limit to $k_2 r_o$. However, for these cases, it is seen that the interaction cross section is quite sensitive to the nuclear radius. Consequently, although the discrepancy could quite easily be due to statistics, a larger nuclear radius or the dominance at high energies of long range force terms would improve the agreement in these cases.

Some credence to the energy dependence found for the mean free path in a previous section is given by the rough agreement between mean free paths as determined by the optical model analysis of the pion-nucleus interaction data with the mean free paths calculated from the pion scattering amplitudes for free nucleons by means of the multiple scattering theory. For the latter calculations, aside from statistical uncertainty of the measured angular distributions, deviations may arise because of the approximations in either the phase shift analysis from the measured angular distributions or the approximations in the multiple scattering. In the case of the phase shifts, Anderson, et al,[16] assumed scattering in the s and p state only and found relatively small scattering in the forward direction according to the derived angular distributions. Consequently, even small contributions from states of higher angular momentum may significantly effect the forward scattering required for the multiple scattering theory. Bodansky, et al,[19] in addition assumed zero scattering in the $T = 1/2$ isotopic spin state. Since the forward scattering is already relatively small, a change in the derived angular distribution with the $T = 1/2$ state included could have a large effect upon the forward scattering.

In the multiple scattering theory, the principal assumptions are the uniform density of nucleons and the lack of correlations between neighboring pairs of nucleons. The former may be expected to be satisfactory except for a possible concentration of protons near the surface of larger nuclei as indicated by deviations from nuclear transition states as predicted by the single particle model of the nucleus. The assumption of a lack of correlation was not investigated here. However, in the example of the effect of the Pauli principle, it is seen that for pion absorption there are few forbidden final states due to the large excess of energy obtained from the pion rest mass.

It was found that in applying the multiple scattering theory the contribution from $\pi^+ + p$ was greater than $\pi^+ + n$ and that the contribution from $\pi^- + n$ was greater than that from $\pi^- + p$. Consequently, for large nuclei with N significantly greater than Z, the interaction cross section for π^- should be larger than that for π^+. Although no calculation was made using the weighted average of N and Z for nuclear emulsion, this probably accounts for the fact that even after the coulomb correction π^- interactions are significantly greater than π^+ interactions in nuclear emulsion as seen in Fig. 21 and Table IV. In Table IV it is seen that the average of b for π^+ and π^- in nuclear emulsions is in good agreement with the result for carbon where N = Z.

In addition to being of some interest in themselves, the results of this experiment and analysis may serve two other purposes. In experiments requiring the identification of pions by their stopping or range, corrections must be made for interaction of the pions in the energy-degrading material. The attenuation cross sections were found in this experiment for a given geometry and are shown in Figs. 13, 14, and 15. From the ring counter cross sections shown in Figs. 16, 17, and 18, attenuation cross sections can be determined for a second geometry of smaller angle. For a sufficiently bad geometry degrader-detector system, i.e., bad geometry with respect to diffraction scattering, the interaction cross section may be used. In this case, at high energies, where the correction is greatest, nuclear area is used. At lower energies, where the correction is considerably less, a cross section smaller than nuclear area is used as seen from Figs. 13, 14, and 15. Where the geometry is "mediocre", the correction is sensitive to the angular distribution of the diffraction scattering. Since

coulomb interference enters in and the effect depends upon the geometry, a detailed study of the correction was not attempted. However, for a rough estimate of the diffraction scattering effect, the Born approximation angular distribution of Eq. (13) may be used with the total scattering cross sections, which may be determined from Figs. 13, 14, and 15. The including of some diffraction scattering will thus increase the attenuation correction.

Another application of the results is to the problem of pion production in complex nuclei where reabsorption has a strong effect. Here a fairly exact treatment may be used. The mean free path for interaction in nuclear matter is taken to be that given by Eqs. (14) and (15) with the constant b given in Table IV. In obtaining this, the interaction mean free path was derived from the effects of the interaction by means of the optical model. To obtain the reabsorption of pions in the production problem, one can derive the effects of the interaction from the interaction mean free path by means of a similar model. For this case the decrease in pion probability amplitude is e^{-x/λ_a} and boundary effects are neglected. Thus, in a sense, the optical model is cancelled out to a certain extent. It can be seen from Fig. 22 that at high pion energies, even the smaller nuclei are quite opaque and a strict $A^{2/3}$ production law should be expected. For fairly low pion energies, however, even the largest nucleus is transparent to a considerable degree and the production cross sections should approach an A dependency, if no other effects contribute.

VII ACKNOWLEDGEMENTS

The encouragement and guidance of Dr. Chaim Richman are gratefully acknowledged. The assistance of Dr. Stanley Leonard throughout the major portion of the experiment contributed greatly to its success. Mr. James Vale and the cyclotron crew are to be thanked for their aid in setting up the apparatus and in making the bombardments.

VIII REFERENCES

1. G. Bernardini, E. T. Booth and L. Lederman, Phys. Rev. 83, 1075 and 1277 (1951).

2. G. Bernardini and F. Levy, Phys. Rev. 84, 610 (1951).

3. H. Bradner and B. Rankin, Phys. Rev. 87, 547 and 553 (1952).

4. A. M. Shapiro, Phys. Rev. 84, 1063 (1951).

5. H. Byfield, J. Kessler, and L. M. Lederman, Phys. Rev. 86, 17, (1952).

6. C. Chedester, P. Isaacs, A. Sachs, and J. Steinberger, Phys. Rev. 82,(1951).

7. R. Martin, Phys. Rev. 87, 1052 (1952).

8. W. F. Cartwright, C. Richman, M. M. Whitehead, and H. A. Wilcox, Phys. Rev. (in press).

9. C. Richman, M. Skinner, J. Merritt, and B. Youtz, Phys. Rev. 80, 900 (1950).

10. W. Dudziak, private communication.

11. E. Fermi, Nuclear Physics (University of Chicago Press, Revised, 1950).

12. L. Schiff, Quantum Mechanics, (McGraw-Hill Book Company, Inc., 1949).

13. S. Fernbach, R. Serber, and T. B. Taylor, Phys. Rev. 75, 1352 (1949).

14. H. L. Anderson, E. Fermi, R. Martin, and D. E. Nagle, Phys. Rev. 91, 155 (1953). D. Bodansky, A. Sachs, and J. Steinberger, Phys. Rev. 90, 997 (1953). P. Isaacs, A. Sachs, and J. Steinberger, Phys. Rev. 85, 803 (1952). E. C. Fowler, W. B. Fowler, R. P. Shutt, A. N. Thorndike, and W. L. Whittemore, Phys. Rev. 91, 135 (1953). C. E. Angell and J. P. Perry, Phys. Rev. 90, 724 (1953). S. Leonard and D. Stork, private communication.

15. M. Lax, Rev. Mod. Phys. 23, 287 (1951).

16. H. L. Anderson, E. Fermi, R. Martin, and D. E. Nagle, Phys. Rev. 91, 155 (1953).

17. E. U. Condon and G. H. Shortly, The Theory of Atomic Spectra (Cambridge University Press, 1935).

18. H. A. Bethe and P. R. Wilson, Phys. Rev. 83, 690 (1951).

19. D. Bodansky, A. Sachs, and J. Steinberger, Phys. Rev. 90, 997 (1953).

20. J. Tracy, University of California Radiation Laboratory Report No. UCRL-2013, Nov. 16, 1952.

21. H. Heckman, University of California Radiation Laboratory Report No. UCRL-2062, Dec. 23, 1952.

22. R. LeLevier, Phys. Rev. 87, 217 (1952).

23. D. C. Peaslee, Phys. Rev. 87, 862 (1952).

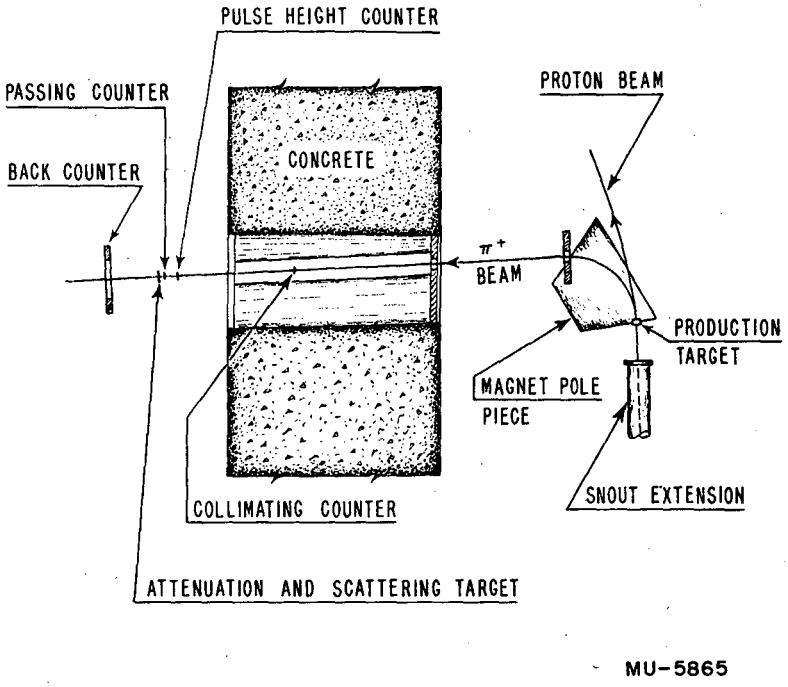

Fig. 1 Physical arrangement.

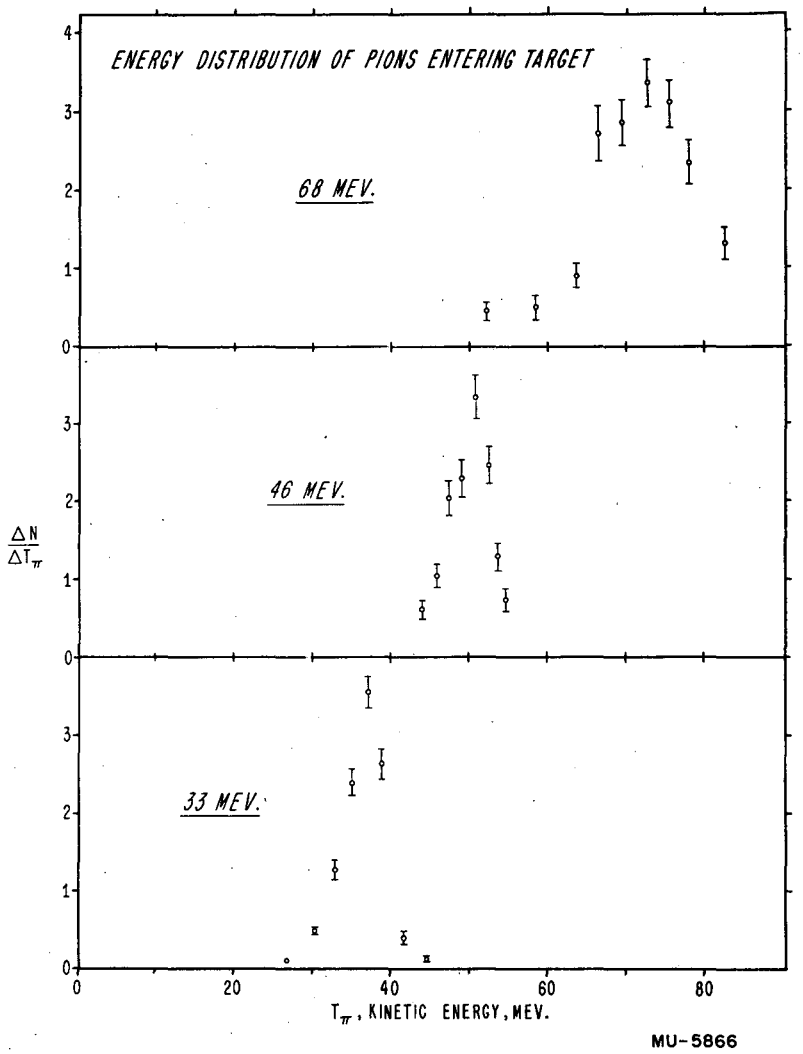

Fig. 2 Energy distribution of the pion beams.

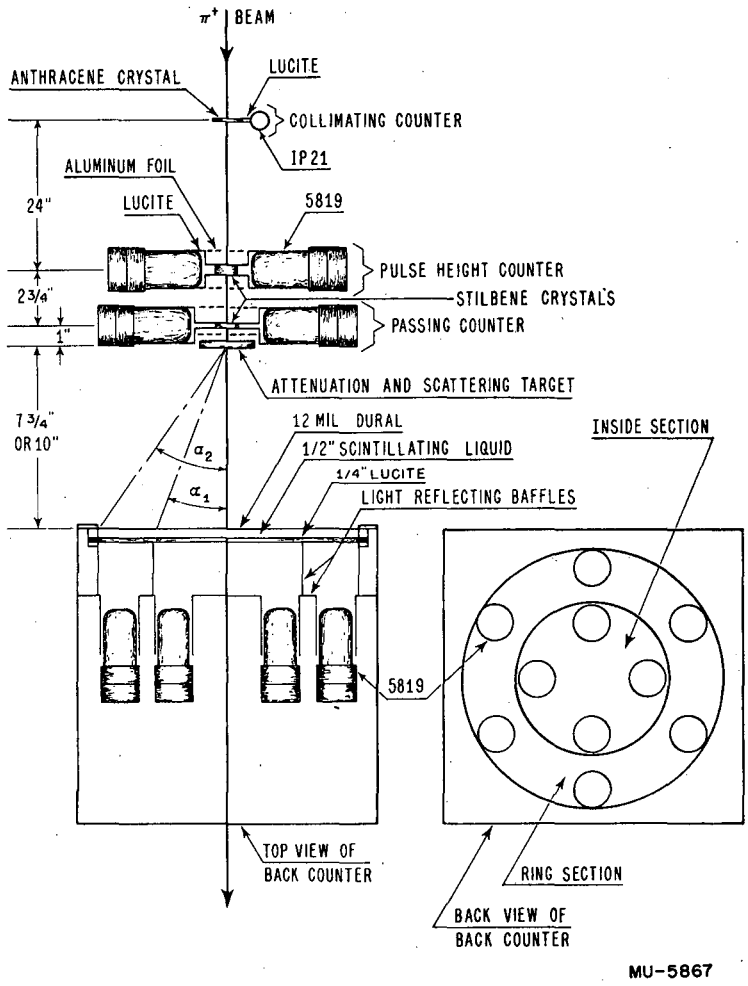

Fig. 3 Detail of the counter system.

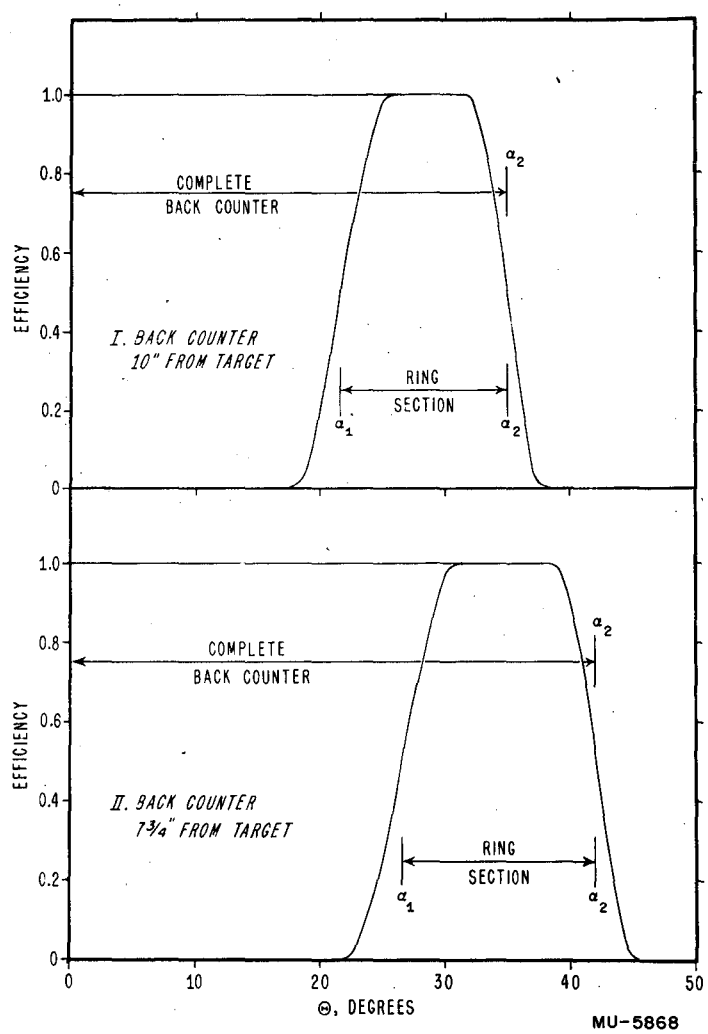

Fig. 4 Angular efficiency of the back counter showing the ring section.

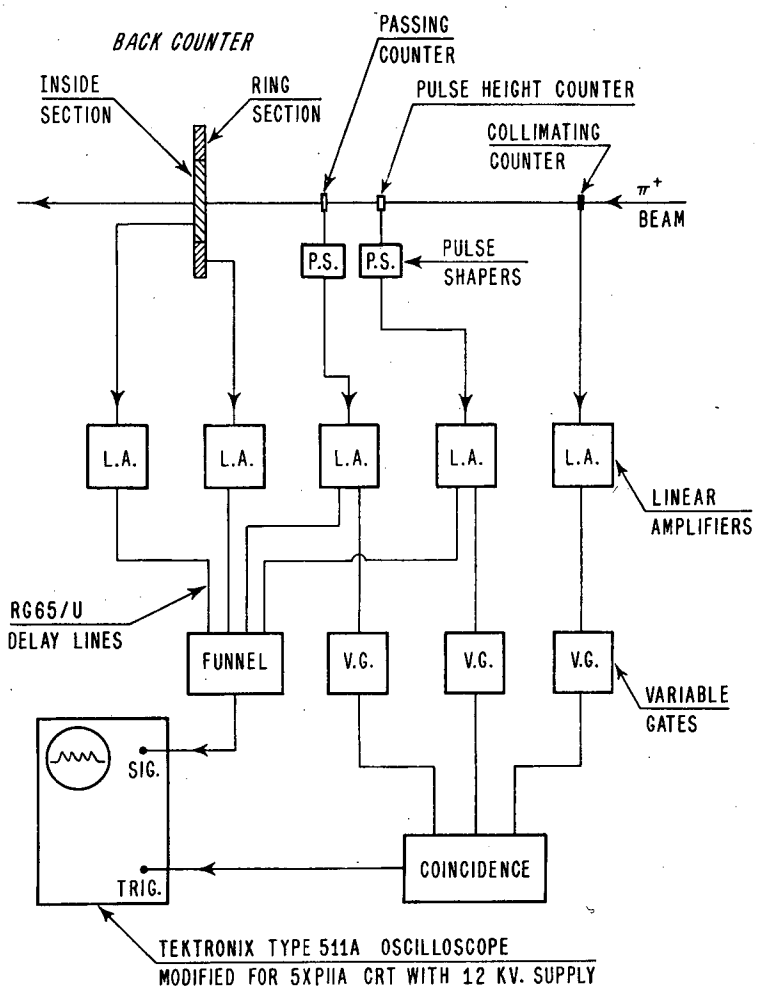

MU-5869

Fig. 5 Schematic diagram of the electronics.

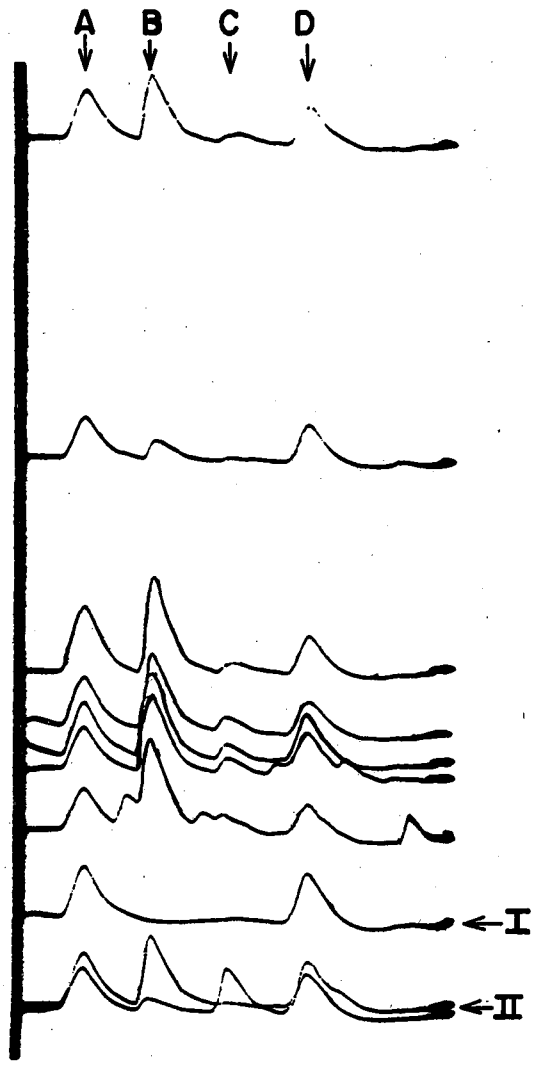

Fig. 6 Typical section of the film showing the pulses on the trace images. Pulse A is from the pulse height counter, B is from the inside section of the back counter, C (when present) is from the ring section of the back counter, and D is the pulse from the passing counter. Trace I is an attenuation event and Trace II is a ring counter event.

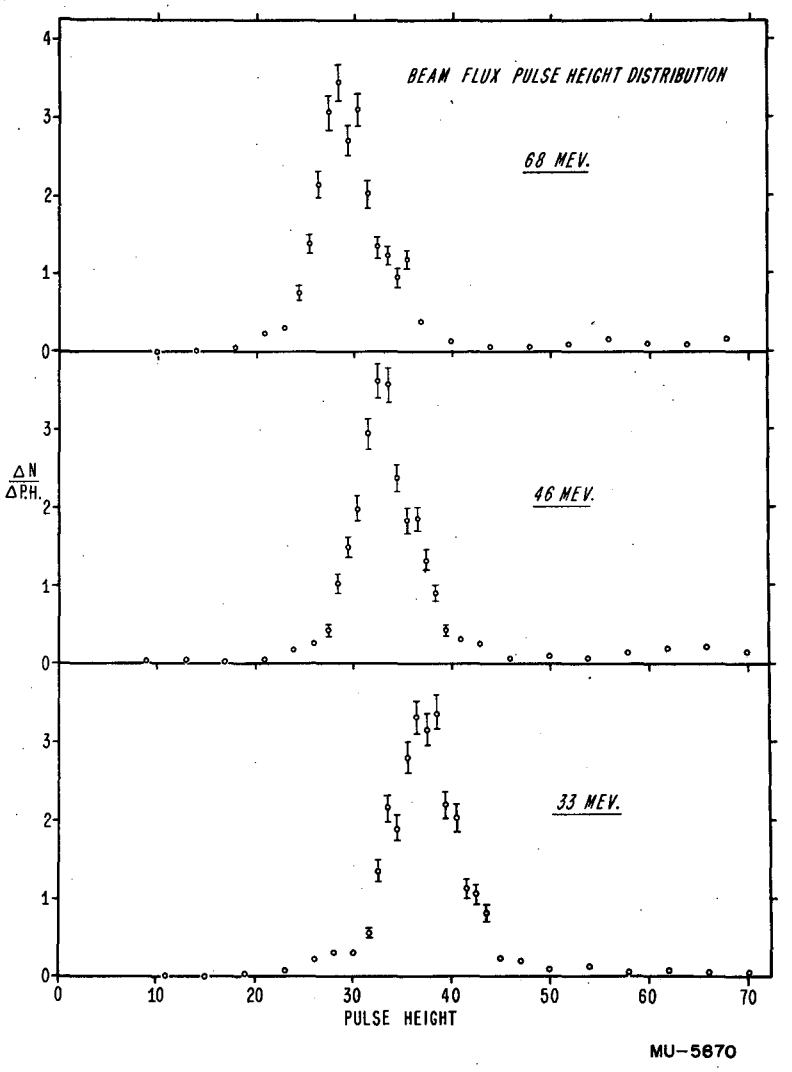

Fig. 7 Pulse height distribution of all particles in the beam at the three pion energies.

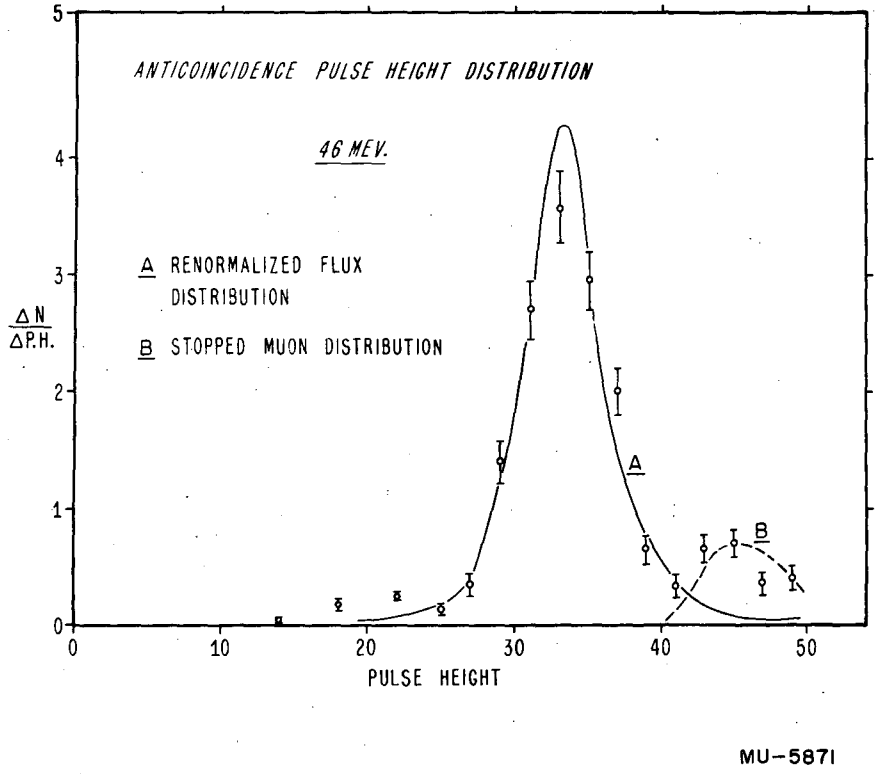

Fig. 8 Pulse height distribution of the attenuation events for the medium energy.

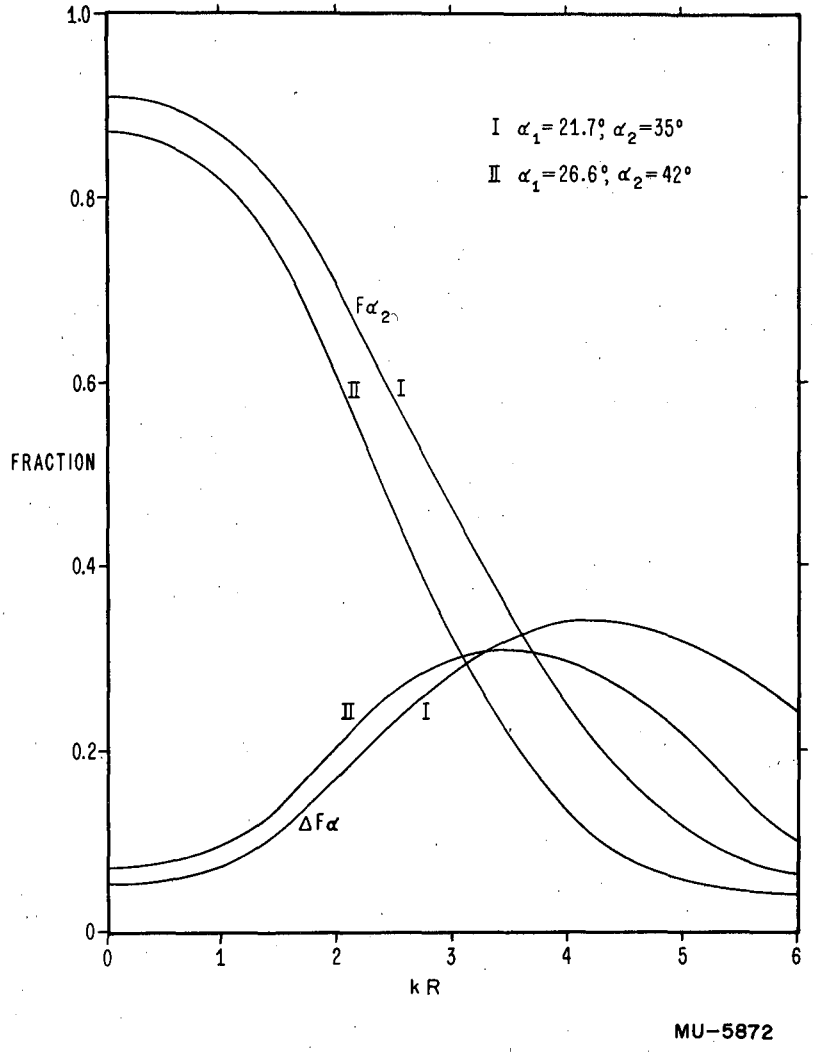

Fig. 9 Fraction scattered into the back counter, $F_{\alpha 2}$, and fraction scattered into the ring counter, ΔF_{α}, for the two geometries used in the experiment.

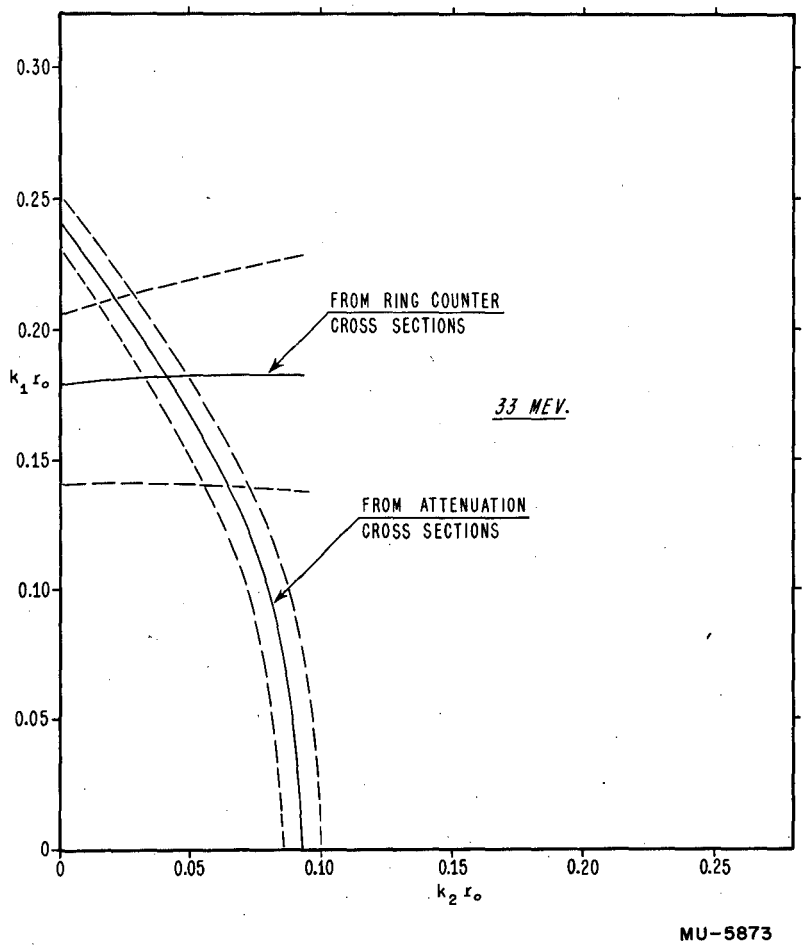

Fig. 10 Sets of parameters, $k_1 r_o$ and $k_2 r_o$, for best fit to the measured attenuation and ring counter cross sections at the low energy.

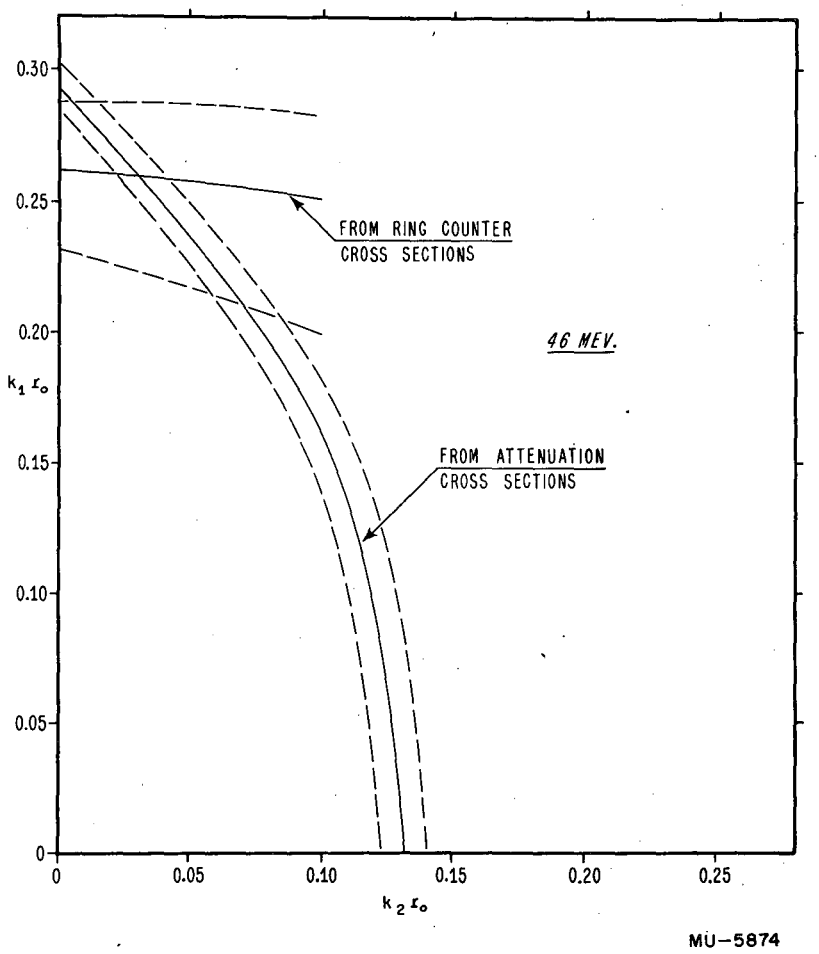

Fig. 11 Sets of parameters, $k_1 r_o$ and $k_2 r_o$, for best fit to the measured attenuation and ring counter cross sections at the medium energy.

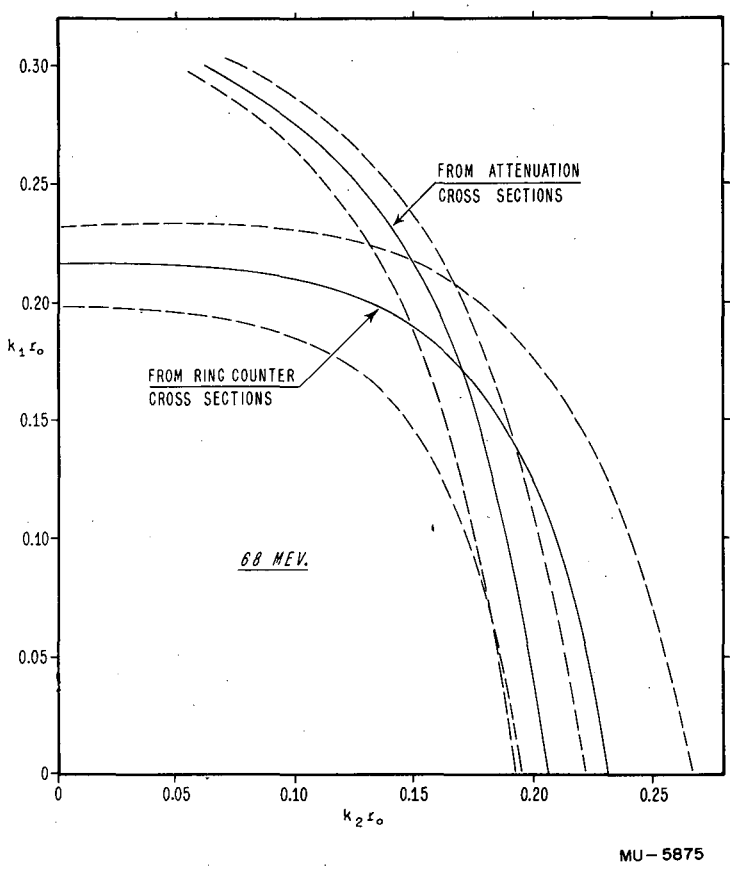

Fig. 12 Sets of parameters, $k_1 r_o$ and $k_2 r_o$, for best fit to the measured attenuation and ring counter cross sections at the high energy.

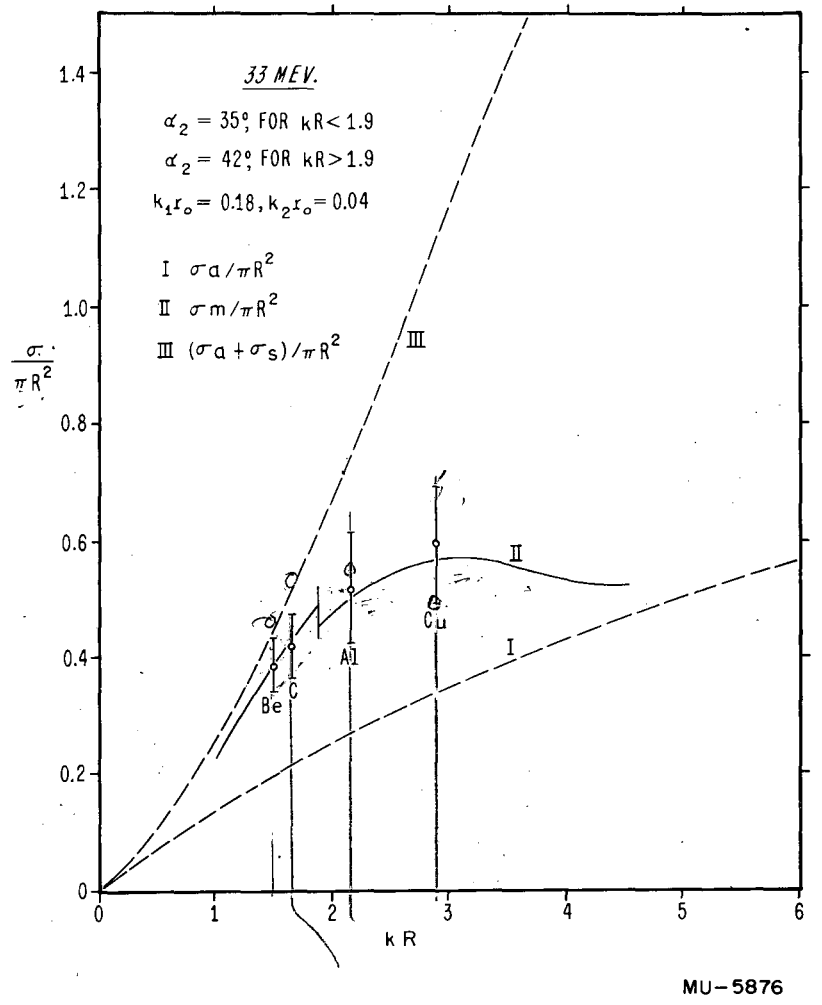

$Y = \cancel{\sigma/A^{1/3}} \sim A^{2/3}$

$\frac{Y}{A^{2/3}} = \approx 1$

$\frac{Y}{A^{2/3}}$

$\sigma \approx A$

Fig. 13 Comparison of the measured attenuation cross sections at the low energy with those calculated by means of the optical model. $k_1 r_o$ and $k_2 r_o$ have the values determined by the intersection of the two curves in Fig. 10.

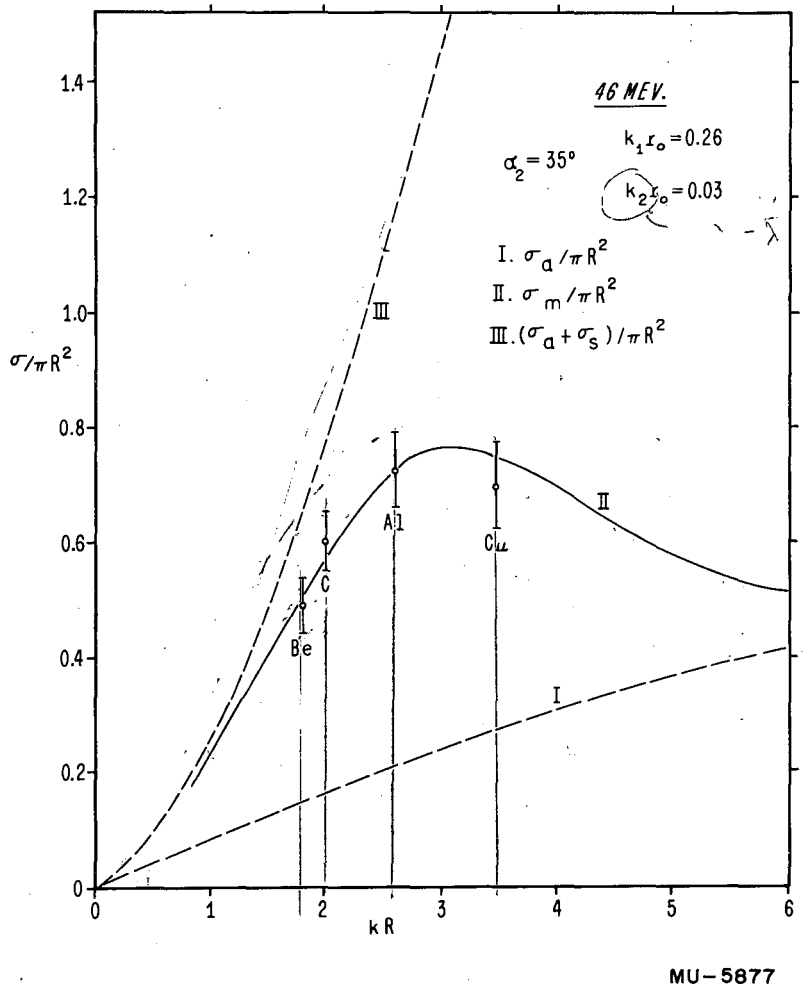

Fig. 14 Comparison of the measured attenuation cross sections at the medium energy with those calculated by the optical model. $k_1 r_o$ and $k_2 r_o$ have the values determined by the intersection of the two curves in Fig. 11.

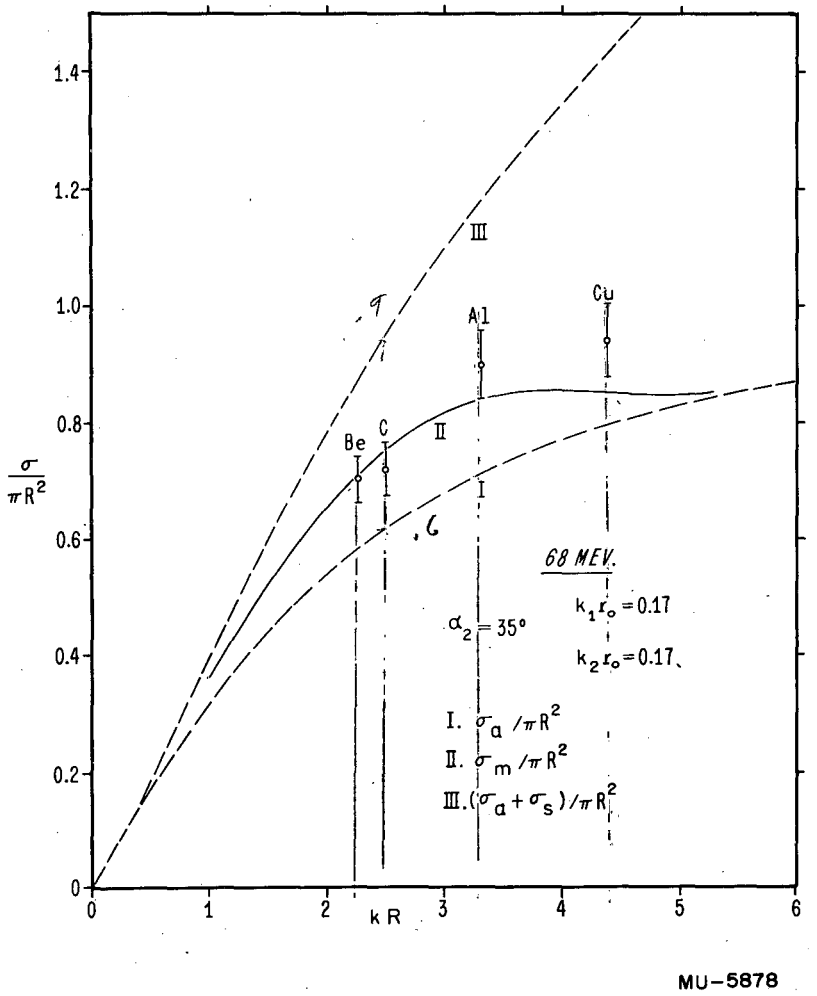

Fig. 15 Comparison of the measured attenuation cross sections at the high energy with those calculated by the optical model. $k_1 r_o$ and $k_2 r_o$ have the values determined by the intersection of the two curves in Fig. 12.

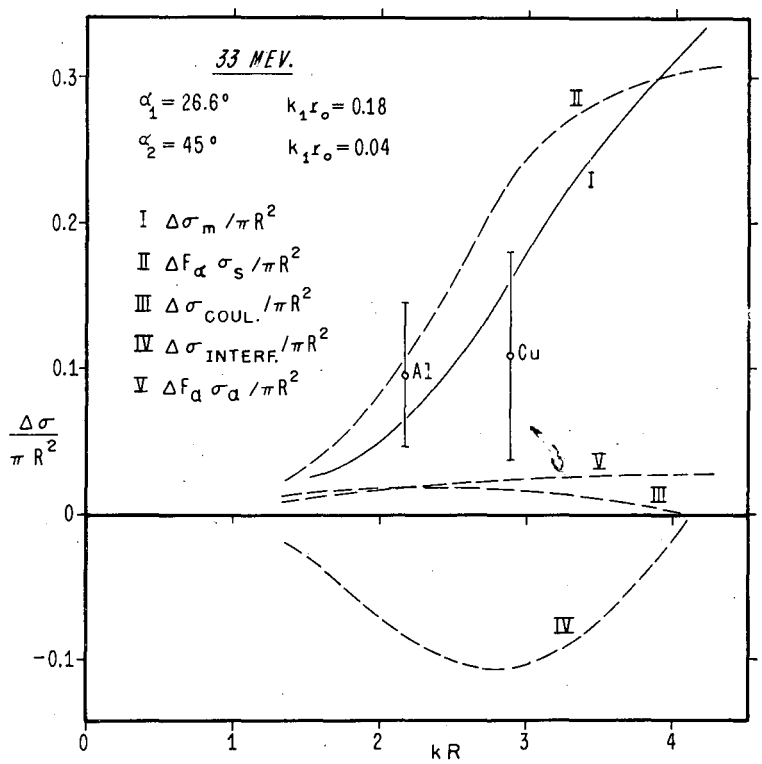

MU-5879

Fig. 16 Comparison of the measured ring-counter cross sections at the low energy with those calculated by the optical model with the coulomb contributions determined from the Born approximation. The values of $k_1 r_o$ and $k_2 r_o$ are those used in Fig. 13.

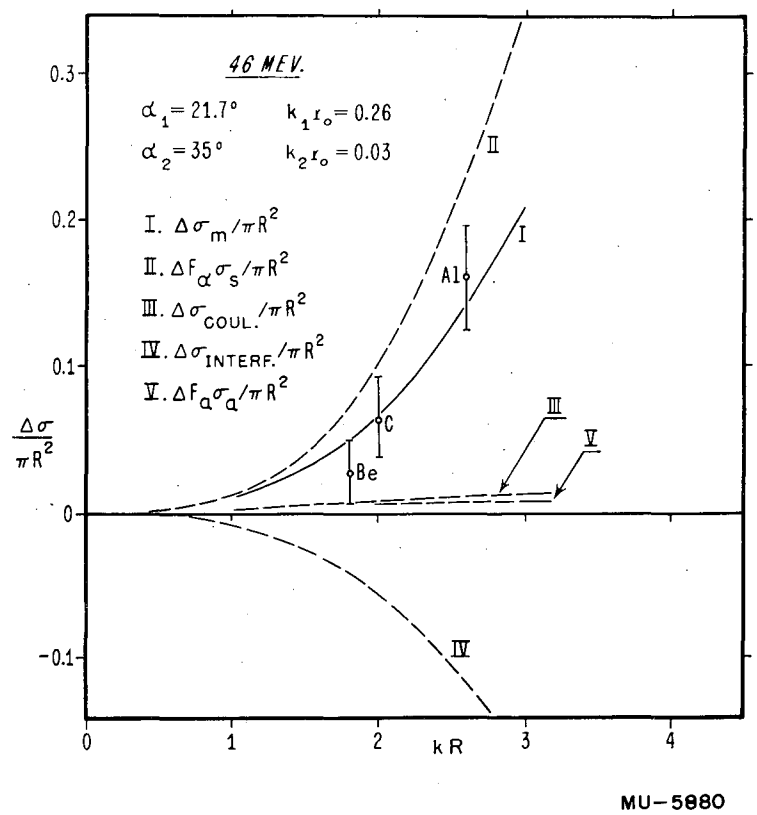

Fig. 17 Comparison of the measured ring counter cross sections at the medium energy with those calculated by the optical model with the coulomb contributions determined from the Born approximation. The values of $k_1 r_o$ and $k_2 r_o$ are those used in Fig. 14.

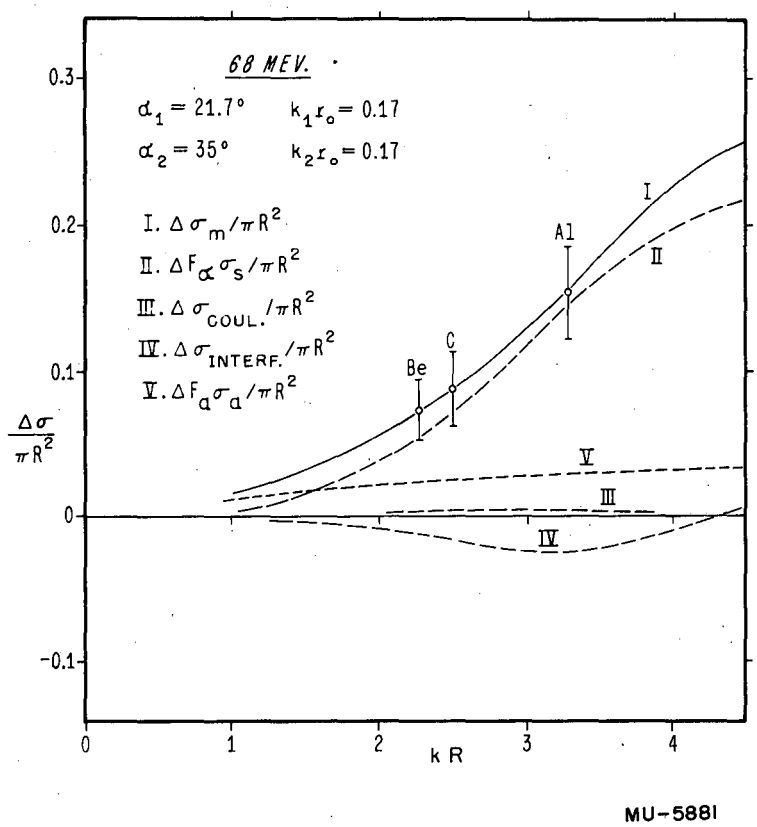

Fig. 18 Comparison of the measured ring counter cross sections at the high energy with those calculated by the optical model with the coulomb contributions determined from the Born approximation. The values of $k_1 r_o$ and $k_2 r_o$ are those used in Fig. 15.

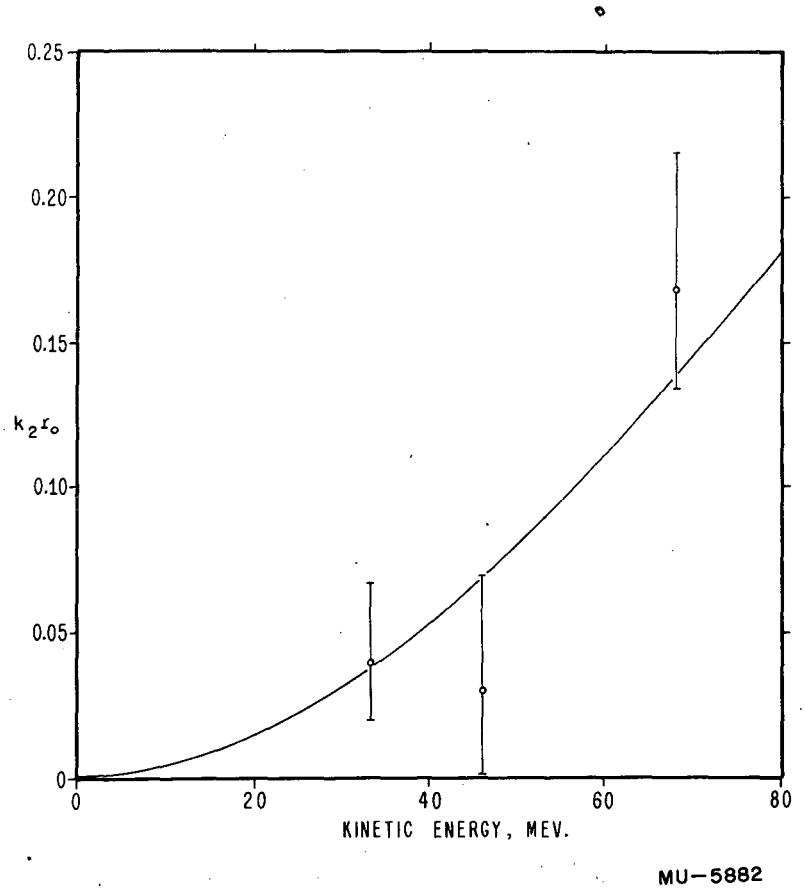

Fig. 19 The interaction parameter, $k_2 r_o$, versus pion energy. The solid curve is from Eq. (14) with a least squares fit giving $b = 0.21^{+0.04}_{-0.03}$.

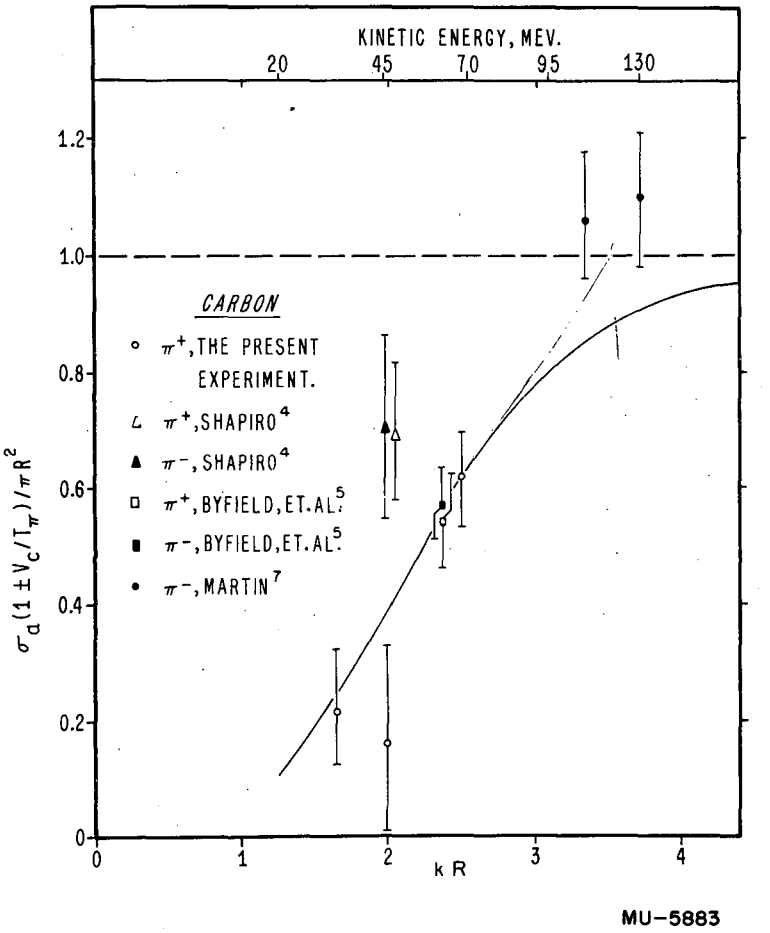

Fig. 20 Carbon interaction cross sections versus kR with the coulomb correction. The solid curve is from Eqs. (6) and (14) with a least squares fit giving $b = 0.26 \pm 0.03$.

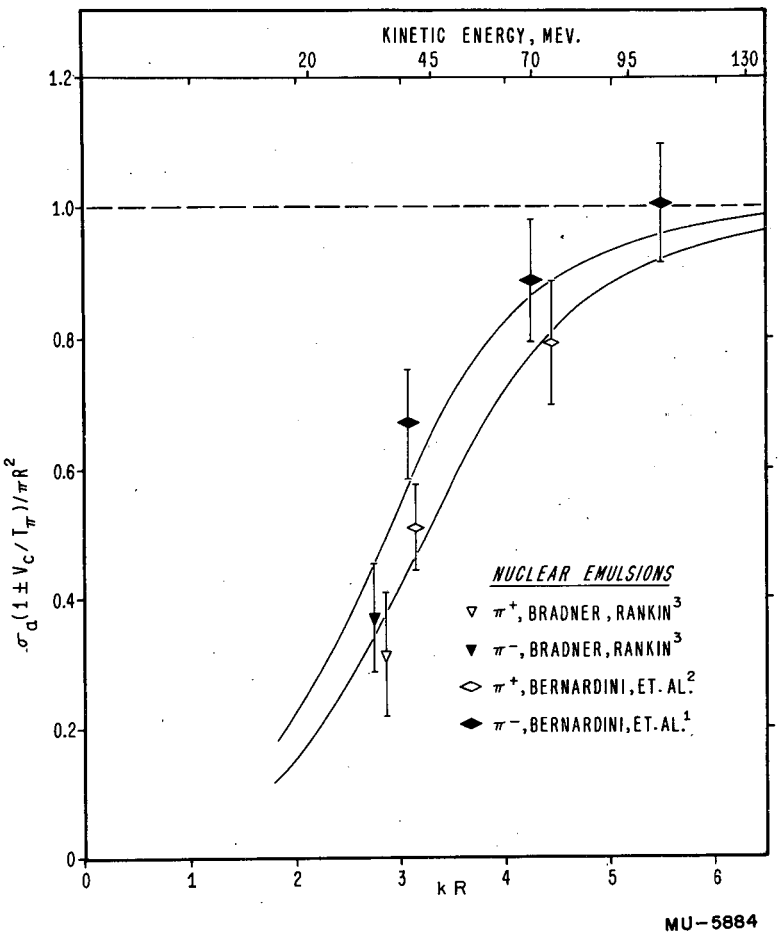

Fig. 21 Nuclear emulsion interaction cross sections versus kR with the coulomb correction. The curves are from Eqs. (6) and (14). The upper curve is for $b = 0.36 \pm 0.07$ determined by a least squares fit to the π^- cross sections. The lower curve is for $b = 0.24 \pm 0.04$ determined by a least squares fit to the π^+ cross sections.

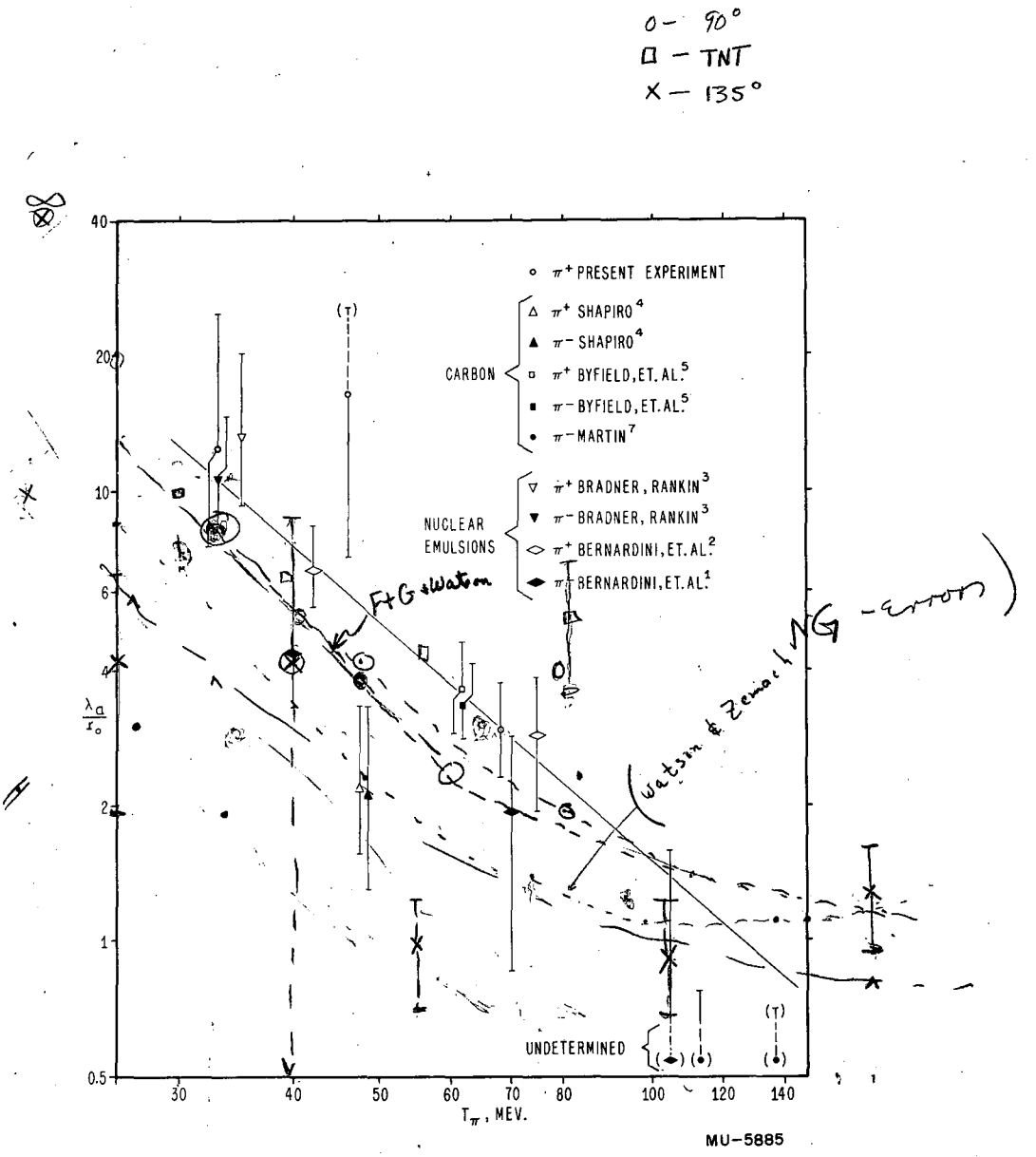

Fig. 22 Interaction mean free paths versus pion energy. The pionts are determined by Eqs. (6) and (15) and the interaction cross section data with the coulomb correction. The solid curve is from Eqs. (14) and (15) with a least squares fit giving b = 0.262 ± 0.023.

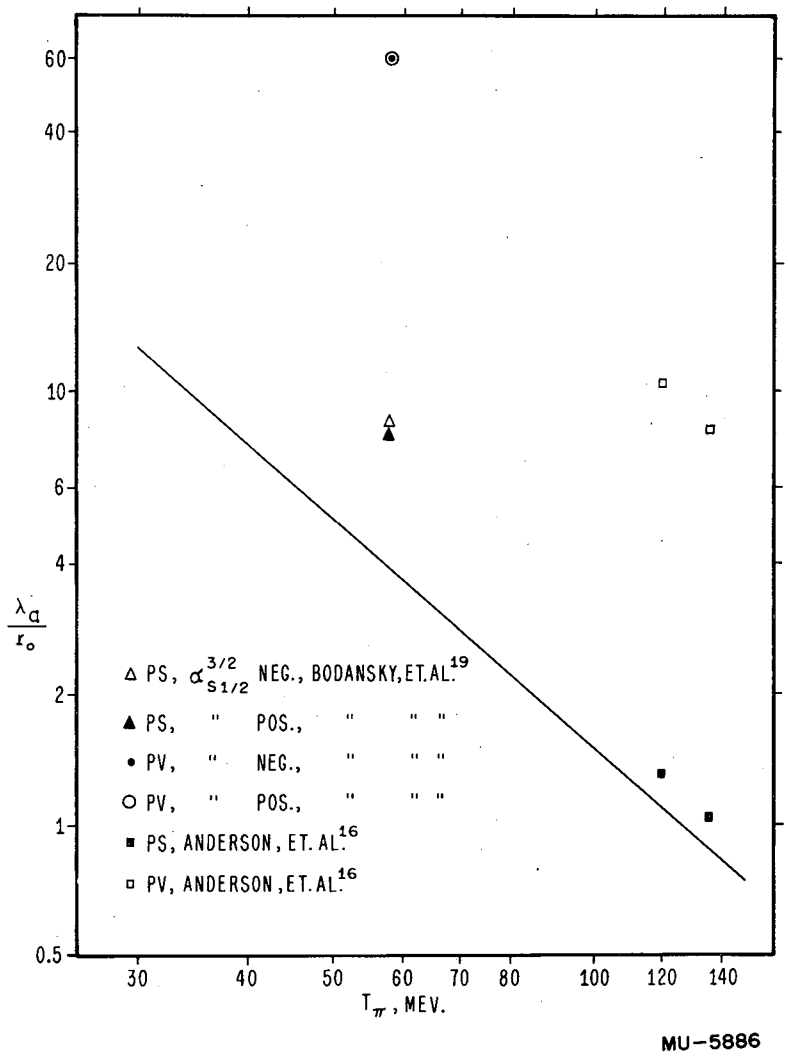

Fig. 23 Interaction mean free paths from the multiple scattering treatment of the pion scattering amplitudes for free nucleons. The solid curve is the same as that in Fig. 22.